



NAVAL POSTGRADUATE SCHOOL

MONTEREY, CALIFORNIA

THESIS

GENERATION OF CLUTTER WITHIN A STRUCTURED TARGET SYNTHETIZER

by

Yowchyun Lin

September 2012

Thesis Advisor:

Second Reader:

Phillip E. Pace

Douglas J. Fouts

Approved for public release; distribution is unlimited

THIS PAGE INTENTIONALLY LEFT BLANK

| | | | | |
|---|---|--|--|--|
| REPORT DOCUMENTATION PAGE | | | <i>Form Approved OMB No. 0704-0188</i> | |
| Public reporting burden for this collection of information is estimated to average 1 hour per response, including the time for reviewing instruction, searching existing data sources, gathering and maintaining the data needed, and completing and reviewing the collection of information. Send comments regarding this burden estimate or any other aspect of this collection of information, including suggestions for reducing this burden, to Washington headquarters Services, Directorate for Information Operations and Reports, 1215 Jefferson Davis Highway, Suite 1204, Arlington, VA 22202-4302, and to the Office of Management and Budget, Paperwork Reduction Project (0704-0188) Washington DC 20503. | | | | |
| 1. AGENCY USE ONLY (Leave blank) | | 2. REPORT DATE September 2012 | 3. REPORT TYPE AND DATES COVERED Master's Thesis | |
| 4. TITLE AND SUBTITLE Generation of Clutter within a Structured Target Synthesizer | | | 5. FUNDING NUMBERS | |
| 6. AUTHOR(S) Yowchyun Lin | | | | |
| 7. PERFORMING ORGANIZATION NAME(S) AND ADDRESS(ES) Naval Postgraduate School Monterey, CA 93943-5000 | | | 8. PERFORMING ORGANIZATION REPORT NUMBER | |
| 9. SPONSORING /MONITORING AGENCY NAME(S) AND ADDRESS(ES) N/A | | | 10. SPONSORING/MONITORING AGENCY REPORT NUMBER | |
| 11. SUPPLEMENTARY NOTES The views expressed in this thesis are those of the author and do not reflect the official policy or position of the Department of Defense or the U.S. Government. IRB Protocol number _____N/A_____. | | | | |
| 12a. DISTRIBUTION / AVAILABILITY STATEMENT Approved for public release; distribution is unlimited | | | 12b. DISTRIBUTION CODE | |
| 13. ABSTRACT (maximum 200 words) <p>This thesis addresses the development of a novel sea clutter module to enhance the digital image synthesizer (DIS) integrated circuit, so that the false-target image generated will be more resistant to the electronic protection used within inverse synthetic aperture radar (ISAR). The modified DIS design proposed incorporates the DIS false target with a sea clutter effect so that the interaction between the reflective surface of the target object and the background clutter is emulated. Furthermore, the random Doppler shift of the sea clutter derived from the novel DIS design can be used to ease the discontinuity in the cross-range domain. The DIS false-target image is then closer to that of a real target. The signal processing for the sea clutter module and the DIS and the ISAR compression of the modulated return are modeled to evaluate the performance of the modified DIS design. Such evaluation is based on investigating the discontinuity of the resultant target image in the cross-range domain and the correlation between the image and the background clutter. Finally, various radar wavelengths and sea states are used to verify the sea clutter is reasonably generated by the module under different environmental conditions. Also, different false-target profiles that represent the target in motion are used to confirm the integrity of the DIS design.</p> | | | | |
| 14. SUBJECT TERMS Digital Image Synthesizer, DIS, Inverse Synthetic Aperture Radar, ISAR, synthetic Aperture Radar, SAR, Digital RF Memory, DRFM | | | 15. NUMBER OF PAGES 83 | |
| | | | 16. PRICE CODE | |
| 17. SECURITY CLASSIFICATION OF REPORT Unclassified | 18. SECURITY CLASSIFICATION OF THIS PAGE Unclassified | 19. SECURITY CLASSIFICATION OF ABSTRACT Unclassified | 20. LIMITATION OF ABSTRACT UU | |

THIS PAGE INTENTIONALLY LEFT BLANK

Approved for public release; distribution is unlimited

**GENERATION OF CLUTTER WITHIN A STRUCTURED TARGET
SYNTHESIZER**

Yowchyun Lin
Major, Air Force of Taiwan
B.S.C.C, The Citatdel Military Institute, 2001

Submitted in partial fulfillment of the
requirements for the degree of

**MASTER OF SCIENCE IN ELECTRONIC WARFARE SYSTEMS
ENGINEERING**

from the

**NAVAL POSTGRADUATE SCHOOL
September 2012**

Author: Yowchyun Lin

Approved by: Phillip E. Pace
Thesis Advisor

Douglas J. Fouts
Second Reader

Dan Boger
Chair, Department of IS Department

THIS PAGE INTENTIONALLY LEFT BLANK

ABSTRACT

This thesis addresses the development of a novel sea clutter module to enhance the digital image synthesizer (DIS) integrated circuit, so that the false-target image generated will be more resistant to the electronic protection used within inverse synthetic aperture radar (ISAR). The modified DIS design proposed incorporates the DIS false target with a sea clutter effect so that the interaction between the reflective surface of the target object and the background clutter is emulated. Furthermore, the random Doppler shift of the sea clutter derived from the novel DIS design can be used to ease the discontinuity in the cross-range domain. The DIS false-target image is then closer to that of a real target. The signal processing for the sea clutter module and the DIS and the ISAR compression of the modulated return are modeled to evaluate the performance of the modified DIS design. Such evaluation is based on investigating the discontinuity of the resultant target image in the cross-range domain and the correlation between the image and the background clutter. Finally, various radar wavelengths and sea states are used to verify the sea clutter is reasonably generated by the module under different environmental conditions. Also, different false-target profiles that represent the target in motion are used to confirm the integrity of the DIS design.

THIS PAGE INTENTIONALLY LEFT BLANK

TABLE OF CONTENTS

| | | |
|-------------|---|-----------|
| I. | INTRODUCTION..... | 1 |
| A. | ISAR AND DRFM JAMMING | 1 |
| 1. | ISAR..... | 1 |
| 2. | Digital RF Memory Jamming..... | 2 |
| B. | PRINCIPAL CONTRIBUTIONS | 3 |
| C. | THESIS OUTLINE..... | 5 |
| II. | IMAGING RADAR FUNDAMENTALS | 7 |
| A. | RANGE AND CROSS-RANGE RESOLUTION..... | 7 |
| B. | ISAR IMAGING PROCESS..... | 10 |
| 1. | Range Compression | 10 |
| 2. | Cross-Range Compression | 11 |
| C. | CHAPTER SUMMARY..... | 12 |
| III. | ISAR ELECTRONIC ATTACK..... | 13 |
| A. | INTRODUCTION | 13 |
| B. | DIGITAL IMAGE SYNTHESIZER..... | 14 |
| 1. | Overview | 14 |
| 2. | Digital RF Memory Phase Samples..... | 15 |
| 3. | False-Target Image Profile..... | 18 |
| 4. | The DIS Signal Processing | 22 |
| 5. | Variant of the DIS Design with Multiple False Targets | 23 |
| C. | CHAPTER SUMMERY | 25 |
| IV. | METHODS TO DISCRIMINATE FALSE TARGETS..... | 27 |
| A. | CONTINUITY OF THE FALSE TARGET IN THE ISAR IMAGE | 27 |
| B. | PULSE DIVERSITY WITH A DRFM PENALIZING ALGORITHM | 29 |
| C. | CROSS-TRACK INTERFEROMETRY | 34 |
| D. | CHAPTER SUMMERY | 38 |
| V. | THE DIS DESIGN WITH A SEA CLUTTER MODULE..... | 41 |
| A. | INTRODUCTOIN OF SEA CLUTTER MODELING | 41 |
| 1. | Gaussian Clutter Model | 42 |
| 2. | Compound K-Distribution Model | 43 |
| 3. | Doppler Spectrum Based on K-Distributed Model..... | 46 |
| B. | CLUTTER GENERATION PROCESSING | 47 |
| 1. | Gain Coefficient Generation | 48 |
| 2. | Phase Coefficient Generation..... | 52 |
| C. | SIMULATION RESULT | 57 |
| 1. | Evaluation on Performance of the Modified DIS Design | 57 |
| 2. | The Impact of Radar Wavelength | 58 |
| 3. | The Impact of Sea State..... | 59 |
| D. | CHAPTER SUMMERY | 61 |
| VI. | CONCLUSION AND REMARKS | 63 |

| | | |
|---------------------------------|----------------------|----|
| A. | CONCLUSION | 63 |
| B. | RECOMMENDATIONS..... | 64 |
| LIST OF REFERENCES | | 65 |
| INITIAL DISTRIBUTION LIST | | 67 |

LIST OF FIGURES

| | | |
|------------|---|----|
| Figure 1. | Block Diagram of Thesis Objectives. | 4 |
| Figure 2. | The Relative Angular Motion of the Target. | 8 |
| Figure 3. | a) Photo of the USS Crockett b) ISAR Image of the USS Crockett (From [12])..... | 9 |
| Figure 4. | ISAR Imaging Compression Process (From [1])..... | 10 |
| Figure 5. | DIS Block Diagram (From [1])..... | 15 |
| Figure 6. | Functional Diagram of DRFM..... | 16 |
| Figure 7. | Range-Doppler Profile Template for A False Target. | 19 |
| Figure 8. | ISAR Image with Multiple False Targets (From [17]). | 24 |
| Figure 9. | Comparison of ISAR Images on Real Target and DIS False Target. | 27 |
| Figure 10. | Simulations on ISAR False Target with Different Doppler Resolutions..... | 29 |
| Figure 11. | Block Diagram for Radar's DRFM Penalization in Range Process. | 30 |
| Figure 12. | Radar Matched Filtered Signal $S_1(t, u_m)$ (From [19])..... | 32 |
| Figure 13. | Jammer Matched Filtered Signal $S_2(t, u_m)$ (From [19])..... | 33 |
| Figure 14. | Jammer-Penalized Output Signal $S_5(t, u_m)$ (From [19])..... | 34 |
| Figure 15. | Flow Diagram of the Dual-Aperture Cross-Track Interferometry Scheme. | 35 |
| Figure 16. | Geometry of the Dual-Aperture Antenna Cross-Track Interferometry (from [15]). | 36 |
| Figure 17. | DIS Block Diagram with Sea Clutter Module. | 48 |
| Figure 18. | Block Diagram of K-Distributed Clutter Generation Process. | 49 |
| Figure 19. | Normalized RCS Versus Grazing Angle from GIT Model for Sea States 1 to 5 (in the Order of Bottom to Top) (From [22])..... | 50 |
| Figure 20. | Normalized Amplitude Range Profile of the Sea Clutter. | 51 |
| Figure 21. | Pulse-to-Pulse Correlation on the Clutter Generated..... | 54 |
| Figure 22. | Amplitude Frequency Spectrum at Range Cell 1. | 55 |
| Figure 23. | Amplitude Frequency Spectrum at Range Cell 5. | 55 |
| Figure 24. | Amplitude Frequency Spectrum at Range Cell 10. | 56 |
| Figure 25. | Amplitude Frequency Spectrum at Range Cell 20. | 56 |
| Figure 26. | ISAR Image Simulation for DIS and Modified DIS..... | 58 |
| Figure 27. | ISAR Image for Modified DIS at Different Radar Wavelength. | 59 |
| Figure 28. | ISAR Image for Modified DIS at Different Sea State. | 60 |

THIS PAGE INTENTIONALLY LEFT BLANK

LIST OF TABLES

| | | |
|----------|---|----|
| Table 1. | Gain Modulation Quantization Table (From [5]). | 21 |
| Table 2. | Upwind Frequency Displacement under Various Sea States..... | 53 |

THIS PAGE INTENTIONALLY LEFT BLANK

ACKNOWLEDGMENTS

I would like to thank Professor Pace for his guidance, motivation, and support throughout this thesis study. My best wishes to the success of the DIS design and future research efforts. I am also thankful to Professor Fouts for his effort in reviewing this thesis. I especially appreciate the support from Mr. Cook, Richard and Ms. Greer, Noelle for providing suggestions to the structure of the thesis and my writing as well. I am certainly proud of being able to work with such an excellent group of people.

I am grateful to the Air Force of Taiwan for giving me the precious opportunity to get a grateful education at the Citadel Military Institute and Naval Postgraduate School.

I am especially thankful to all friends for their supports throughout my stay in Monterey.

THIS PAGE INTENTIONALLY LEFT BLANK

I. INTRODUCTION

A. ISAR AND DRFM JAMMING

1. ISAR

Inverse synthetic aperture radar (ISAR) is a well-known technology for constructing high-resolution images of moving targets such as ships and aircraft. These high-resolution images, usually in the range and the cross-range (Doppler) domain, represent the reflectivity function of the target as a function of range and depend on the pulse-to-pulse phase coherence of the reflected returns. The image the ISAR generates is the result of coherent processing of the return echoes received at various viewing angles as the target rotates within the radar's field of view [1].

In order for the ISAR to obtain a clear target image, the movement of the target must be significant with respect to the resolving ability of the ISAR. Normally, the motion of the target can be further divided into translational motion, the linear change in distance along a direction between the target and the radar, and rotational motion, the angular change between the target and the radar. In an ISAR range and cross-range (Doppler) image, the range resolution is directly related to the bandwidth of the transmitted waveform, while the cross-range (Doppler) is obtained from the Doppler frequency gradient generated by the relative rotation of the target and depends on the number of pulses integrated.

The 2-D image consists of resolution cells that contain estimates of the magnitude and position of the target scattering surfaces both range and cross-range (Doppler). The change in translational motion can be compensated for in the ISAR image processing, once it is determined. The Doppler frequency produced by a range-resolved scatterer is proportional to the rotation rate of the target and the cross-range distance between the scatterer and the center of the target rotation. The orientation of the range-Doppler image is determined by the target rotation relative to the ISAR. The range dimension is oriented along the radar line-of-sight (LOS) [2,3].

Each reflective return is correlated with a range independent reference function that is determined by the transmitted chirp waveform so that the range information contained within the pulse is resolved [1]. The range-resolve pulse is then processed through an azimuth compression to further extract the Doppler information to construct the range-Doppler image. The easiest approach to perform azimuth compression is to perform a Fourier transform on the range-resolved pulses. In an actual system, the azimuth compression is somewhat more complicated and includes estimating the rotational motion during data collection and then calculating the compression coefficients that give the sharpest focus.

ISAR imaging has become more critical in such global military operations such as target classification, recognition, and identification. Systems like the U.S. AN/APS-137B(V)5 radar and the Russian Sea Dragon maritime patrol radar are capable of adopting an ISAR imaging mode to detect, classify, and track targets over sea and air [4,5]. They provide the target's range, bearing, and positional data with both medium- and high-resolution images for display and recording. Also, due to the ISARs capability for high-resolution imaging, it is extremely beneficial to incorporate the ISAR into the launching program of weapon systems to perform target identification and location during the pre-launch phase of engagement for higher aim point accuracy and probability of kill.

2. Digital RF Memory Jamming

Actions taken to confuse or deceive pre-launch weapon designation and targeting efforts are known as counter-targeting techniques. Counter-targeting actions include the use of low radar cross-section materials on the exterior of the target object, as well as stealth and deception devices. The use of low radar cross-section material reduces the energy of the pulse return to the radar. Stealthy maneuvering lowers the probability of detection, while deception devices tend to confuse the targeting system. The purpose of the actions mentioned above is to prevent the enemy's weapon systems from executing a

targeting process and valid lock-on so that a missile will either fail to be launched or will miss its target. Unfortunately, these actions are largely ineffective against wideband imaging radars like ISAR [6,7].

The development of digital false-target image synthesizer (DIS) circuits to counter ISAR systems were proposed in the late 90s and have been studied continuously ever since. The implementation of the DIS takes advantage of readily available digital radio frequency memory (DRFM) technology in which radio frequency and microwave signals are sampled and stored at high speed. Together, all these DRFM characteristics make it possible for the DIS to change its coefficients and create different structured targets adaptively in real-time [4,6]. Consequently, beyond sampling and storing signals, DRFM systems also recreate the intercepted radar signals to deceive hostile imaging radar systems.

To jam or create false targets against the ISAR, the DIS circuit first modulates the intercepted signals fed from the DRFM (in the form of digitized samples of the chirp pulses in amplitude and in phase) to recreate the scattering effect of a desired false target. Then, the DIS outputs those modulated signals through a digital-to-analog converter to a radio frequency (RF) module, where the signal is frequency up-converted and transmitted to the victim ISAR. Once the ISAR collects the modulated pulses generated by the DIS and coherently processes them to form an image, the outcome is a two-dimensional image that tends to contain the movement of a false target image. Note that a DRFM alone cannot perform the complex modulations required to synthesize large false targets.

B. PRINCIPAL CONTRIBUTIONS

The principal work done within this thesis is described in the block diagram shown in Figure 1. The major tasks completed are described as follows.

The first task completed in this thesis was to perform an IEEE literature search to investigate the ISAR and SAR methods that have been proposed to discriminate the DIS false targets from the real targets. These discrimination techniques allow the ISAR to protect itself from being deceived by structured false targets that are generated by DRFMs. This electronic protection (EP) allows the ISAR to reject the false targets.

Included in this investigation are the image discontinuity, pulse diversity, and cross-track interferometry techniques. The next task is to develop a sea clutter module that works with the DIS and determine how well the new DIS design can defeat the image discontinuity EP techniques used by these types of imaging radar.

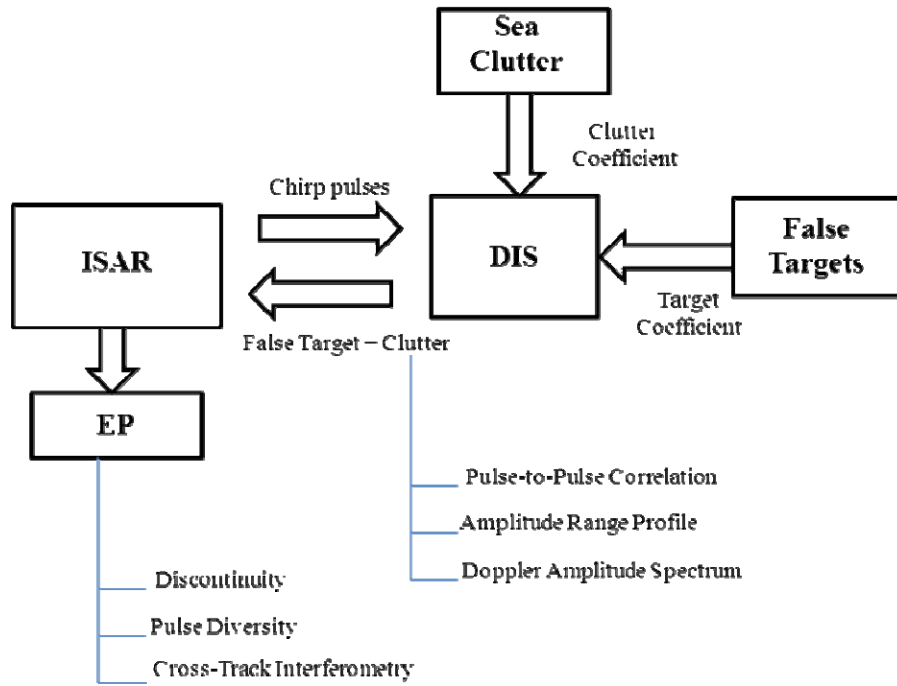


Figure 1. Block Diagram of Thesis Objectives.

The second objective achieved is to study the performance of adding the sea clutter module to the DIS to be used against the ISAR that is capable of false target discrimination. The fundamentals of DRFM operation are also investigated for a better understanding of how the DIS takes advantage of the DRFM architecture to achieve deceptive jamming, or electronic attack (EA), through the creation of structured false targets.

The technique involves calculating and generating the correct sea clutter and represents an important contribution to the DIS design. The DIS signals are pulse-to-pulse correlated with background clutter so that the false target is less vulnerable to the

ISAR correlated image process. Meanwhile, the false target is added with random Doppler shifts so that the false target becomes more realistic and cannot be discriminated by the image discontinuity EP techniques.

In order to generate the sea clutter, the following task is to investigate the statistical models utilized to describe the behavior of the sea clutter, including the Gaussian model, non-Gaussian model, K-distribution model and Weibull model. Of all the models investigated, the K-distribution model is most appropriate since it is able to incorporate both the small and large clutter profile structures. For the purpose of generating the K-distributed sea clutter, the set of statistical random processes such as the Gaussian and gamma random function are used. Upon creation, the clutter is analyzed by examining the Doppler amplitude spectrum and amplitude range profile. The pulse-to-pulse correlation is also examined.

Modeling and simulation of the new DIS design is performed for several scenarios and the resulting DIS false-target image is compared with that of the previous DIS design to investigate how well the performance is improved. In addition, simulation of the sea clutter under various sea state conditions is performed and compared to verify that the random process adopted is acceptable. Both the coherent properties and Doppler profile are also examined.

C. THESIS OUTLINE

Chapter II describes the synthetic image processing of ISAR.

Chapter III explains of how the DIS generates false targets to jam the ISAR.

Chapter IV describes the three types of EP that can discriminate the false targets from the real ones.

Chapter V presents the new sea clutter module that is incorporated with the DIS. The performance of such a module is also evaluated through software simulations in the MATLAB program.

Chapter VI contains conclusions about this thesis and recommendations for future study in related fields.

THIS PAGE INTENTIONALLY LEFT BLANK

II. IMAGING RADAR FUNDAMENTALS

A. RANGE AND CROSS-RANGE RESOLUTION

An imaging radar such as SAR or ISAR is able to provide a high-resolution target image, in both range and cross-range dimensions, at long distance and in bad weather. In SAR, the target is assumed stationary and the radar is in motion, while in ISAR, the target motion provides the changes in relative velocity that cause different Doppler shifts to occur across the target [8,9].

Both types of radar have the same capability to resolve an image in range with the range resolution [5]

$$d_r = \frac{c}{2\Delta} \quad (2.1)$$

where c is the speed of light, and Δ is the bandwidth of the radar chirp pulse. The transmitted chirp pulse can be expressed as [10]

$$s(t) = \text{rect}\left(\frac{t}{T}\right) \exp(j\pi(2f_c t + Kt^2)) \quad (2.2)$$

where $K = \Delta / t_m$ and t_m is the modulation period. To resolve an image in cross-range dimension, however, SAR has a theoretical cross-range resolution

$$d_{a\text{SAR}} = \frac{D}{2} \quad (2.3)$$

where D is the horizontal dimension of the radar aperture. From (2.2), it is clear that the motion of moving targets (i.e., ships that generate complicated motion such as roll, pitch, and yaw over the sea surface) is not taken into consideration. This can result in a serious distortion and displacement from the target's true location in the SAR imaging process. Therefore, SAR is mostly used to recognize stationary objects.

Unlike SAR, ISAR takes advantage of the target's rotation to obtain the resolution in cross-range domain. The cross-range resolution of ISAR is expressed as [5]

$$d_{aISAR} = \frac{\lambda}{2\psi} \quad (2.4)$$

where λ is the ISAR wavelength, and ψ is the relative angular motion of the target during the ISAR observation time, as shown in Figure 2.

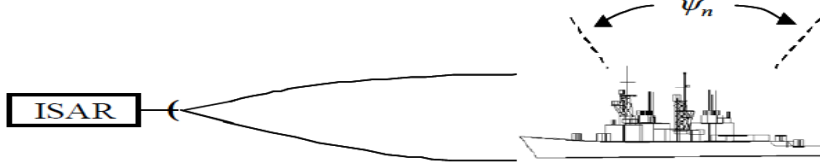


Figure 2. The Relative Angular Motion of the Target.

From (2.3), it is shown that cross-range resolution depends on the amount of angular rotation of the target during the radar observation time when the pulses are collected. The relative angular rotation from each part of the moving target can produce different ISAR cross-range, Doppler resolutions, especially when there is a tremendous rotation in roll, yaw, or pitch.

The pitch motion of a ship causes the top of the mast to have a larger angular motion than the bottom of the mast or the superstructure. These differences cause different Doppler shifts in the cross-range resolution. Along with the conventional range resolution, a vertical profile of the target along its length dimension is generated, which allows the ship to be imaged. Roll motion provides the information about the width of the ship. Compared to the length of the ship, the width information is usually less significant for recognition. Yaw motion of the ship gives a plan view of the target [11].

As the ship moves, its angular rates of motion in pitch, roll, and yaw direction are not generally known. Consequently, the ship length and height cannot be determined since the ISAR result is only a range-Doppler image. An example of ISAR image is shown in Figure 3.

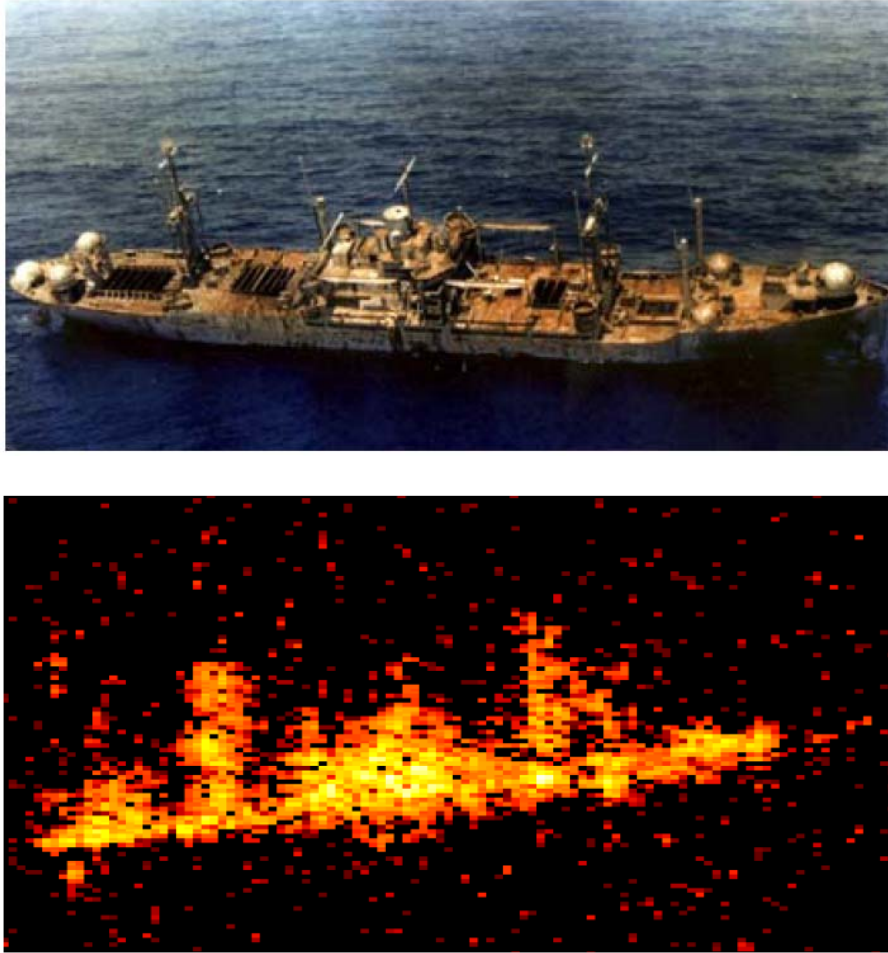


Figure 3. a) Photo of the USS Crockett b) ISAR Image of the USS Crockett (From [12]).

Figure 3a shows a picture of the USS Crockett and Figure 3b shows its equivalent ISAR image taken by an AN/APS-137. It can be concluded by a comparison of the two images that the airborne ISAR was heading directly to the bow of the ship when the image was generated. Notice that the length of the superstructure of the ship in both images is about the same. Also, notice that two masts shown in the ISAR image can be clearly differentiated from the superstructure. The length of the superstructure, the number of masts, and the position of the masts are the key characteristics on which an experienced operator relies for ship recognition [11].

B. ISAR IMAGING PROCESS

1. Range Compression

Pulse compression is a technique adopted to improve the performance of the linear frequency modulated (LFM) ISAR waveform. Both stepped frequency and LFM can be used. However, LFM is the most popular. The returning pulse at the ISAR receiver is compressed to a shorter pulse width $\tau = 1/\Delta$, so that the range resolution is improved by a factor of T/τ , which is the so-called pulse compression ratio. The received pulse is detected, sampled, digitized, and then compressed as shown in Figure 5.

Figure 4 is an example that depicts how an ISAR performs the pulse compression process in range and in cross-range.

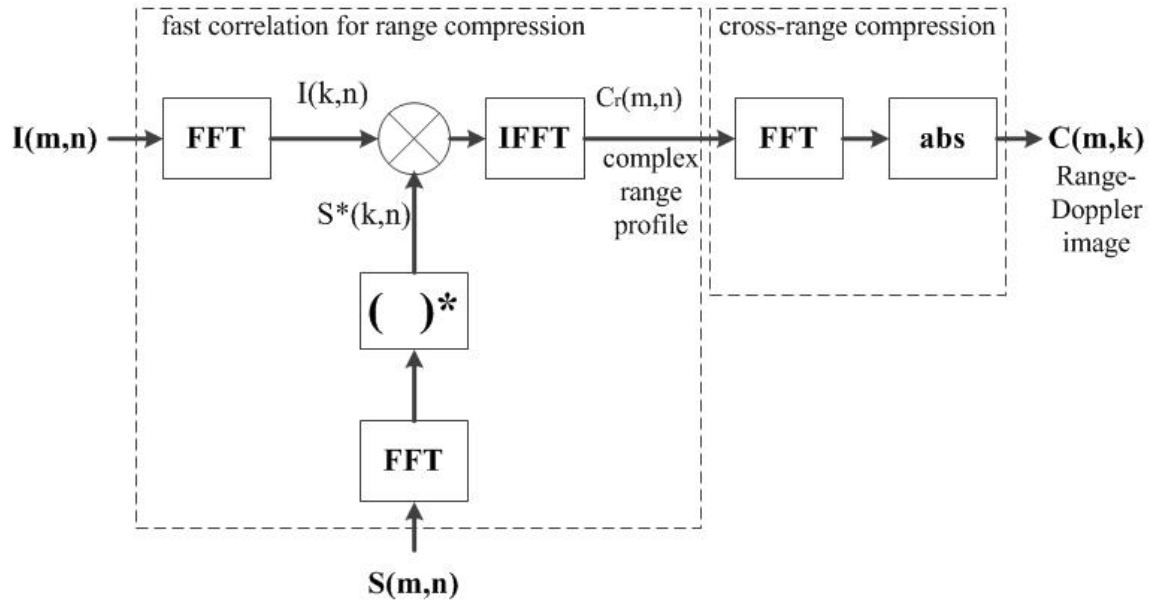


Figure 4. ISAR Imaging Compression Process (From [1]).

The range profile $C_r(m,n)$ for a received pulse is obtained from the cross-correlation of the received signal with the transmitted signal

$$C_r(m,n) = I(m,n) \otimes S(m,n) \quad (2.5)$$

where $I(m,n)$ represents the signal received by ISAR, $S(m,n)$ represents the coherent reference signal derived from the transmitted chirp pulse, and \otimes represents the cross-correlation process. According to the correlation theorem, the discrete Fourier transform (DFT) of the cross-correlation is equivalent to the product of the Fourier transform, such that [5]

$$\mathbb{F}\{I(m,n) \otimes S(m,n)\} = I(k,n) \cdot S^*(k,n) \quad (2.6)$$

To speed the process up, a fast correlation process is used. In (2.5), $I(k,n)$ represents the output of a Fast Fourier Transform (FFT) of $I(m,n)$ as [1]

$$I(k,n) = \mathbb{F}\{I(m,n)\} \quad (2.7)$$

and $S^*(k,n)$ is the complex conjugate equivalent of $S(k,n)$, the output of FFT of $S(m,n)$ as shown below

$$S^*(k,n) = \left(\mathbb{F}\{S(m,n)\}\right)^* \quad (2.8)$$

Then, the range profile can be obtained by taking the inverse DFT of (2.5), which in turn, takes the DFT of the multiplication of (2.6) and (2.7), and thus (2.4) can be rewritten as

$$C_r(m,n) = \mathbb{F}^{-1}\{I(k,n) \cdot S^*(k,n)\} \quad (2.9)$$

At this point, the received signal is said to be range-resolved for each pulse and ready to be further resolved in cross-range for which the Doppler information can be determined.

2. Cross-Range Compression

The azimuth compression is accomplished by Fourier transforming the resolved range profile obtained from N_p pulses. The N_p profiles can be arranged in a matrix as

$$C_r(m, n) = \begin{bmatrix} C_{rN_p}(m, n) & \text{for pulse } N_p \\ C_{rN_p-1}(m, n) & \text{for pulse } N_p - 1 \\ \vdots & \\ C_{r2}(m, n) & \text{for pulse } 2 \\ C_{r1}(m, n) & \text{for pulse } 1 \end{bmatrix} \quad (2.10)$$

where each row corresponds to a returned pulse and each column is comprised of profile elements from the same range bin [5].

The process of azimuth compression is basically the FFT of the time history, or the columns in (2.9), of range profiles, and can be expressed as

$$C(m, k) = \mathbb{F}\{C_r(m, n)\} \quad (2.11)$$

In other words, each time-indexed row expression in (2.9) is transformed to its corresponding frequency-indexed expression, and essentially yields the ISAR range and cross-range image.

C. CHAPTER SUMMARY

The concept of ISAR imaging is briefly presented and explained in terms of its range and cross-range resolution. Next, the LFM ISAR image compression process model proposed in [1] and [5] is introduced as an example of how the received pulse is processed to generate an image. The mathematical expression for both the range compression and the cross-range compression process are also included in the discussion.

In next chapter, the EA techniques used against an ISAR system are examined.

III. ISAR ELECTRONIC ATTACK

A. INTRODUCTION

In modern electronic warfare, the idea of EA is to employ weapon systems or devices to prevent the enemy from utilizing the electromagnetic spectrum. Using weapons or devices to destroy the enemy's equipment is usually referred to as a "hard-kill," while adopting jamming devices to deny or degrade the ability of a radar system to obtain target information like range, velocity, and angle and tracking is referred to as soft-kill techniques [13].

There have been many efforts devoted to researching different types of jamming techniques to defeat ISAR high-resolution imaging capability. Most of the methods proposed are divided into two categories: noise jamming and deception jamming. The major difference between noise jamming and deception jamming is on the correlation between the jamming signal and the real target return.

The objective of noise jamming is to inject an interference signal into the victim radar receiver such that the actual return is completely overwhelmed by the interference. In order to perform noise jamming, a jammer has to continuously generate noise that can be either modulated in amplitude or in frequency [14].

At the victim radar receiver, the ISAR return signal is weaker in energy compared to the noise. Although the noise signal does not compress like the target signal does, it can still distort the image classification process. The loss of information on the target affects the ISAR motion compensation process and can also distort the resulting range and cross-range image quality. Since random noise is completely decorrelated with respect to the compression process within the ISAR receiving system. Noise jamming is not as effective as one might expect against ISAR [13].

The goal of deception jamming is to mask the real target by sending suitable modified replicas of the real return to the victim radar so that those replicas can go through the radar's signal processing and create a false target to confuse the radar. The deception signal transmitted by a jammer basically contains certain inter-pulse

information of the ISAR returning signal and has more correlation with the return signal [15]. As a result, the deception signal can get through the ISAR imaging process and generate a realistic false-target image, which leads to ineffective decision-making by the radar, radar operator, or even commanding officer. Deception jamming is generally considered as an economic and effective method against ISAR compared to noise jamming and will be the technology discussed in this chapter and throughout this thesis.

B. DIGITAL IMAGE SYNTHESIZER

1. Overview

The digital image synthesizer (DIS), proposed in [1] and fabricated and tested in [16], is a pipelined, all-digital image synthesizer designed to deceive LFM ISARs of various carrier frequencies. The essential concept of operation is to emulate false-target signals and transmit those false signals back to the ISAR so that a false target is generated on the resulting range-Doppler image at the end of imaging process.

As an application of deceptive electronic attack, the power of the false-target signal should be high enough to cover the true ISAR return and low enough to avoid the saturation of the ISAR receiver, which otherwise could possibly reveal the presence of jamming. Also, in order to effectively deceive an ISAR, the false-target signals must be appropriately generated such that they are realistic in size and in Doppler effects to reflect a feasible target size and motion.

With the help of modern digital signal process techniques, such as high-performance DRFMs, it is possible to enhance the false-target signal with proper phase and gain modulations by integrating information including range, Doppler and radar cross-section (RCS) into the intercepted ISAR pulses before retransmitting. A block diagram of the DIS architecture is shown in Figure 5.

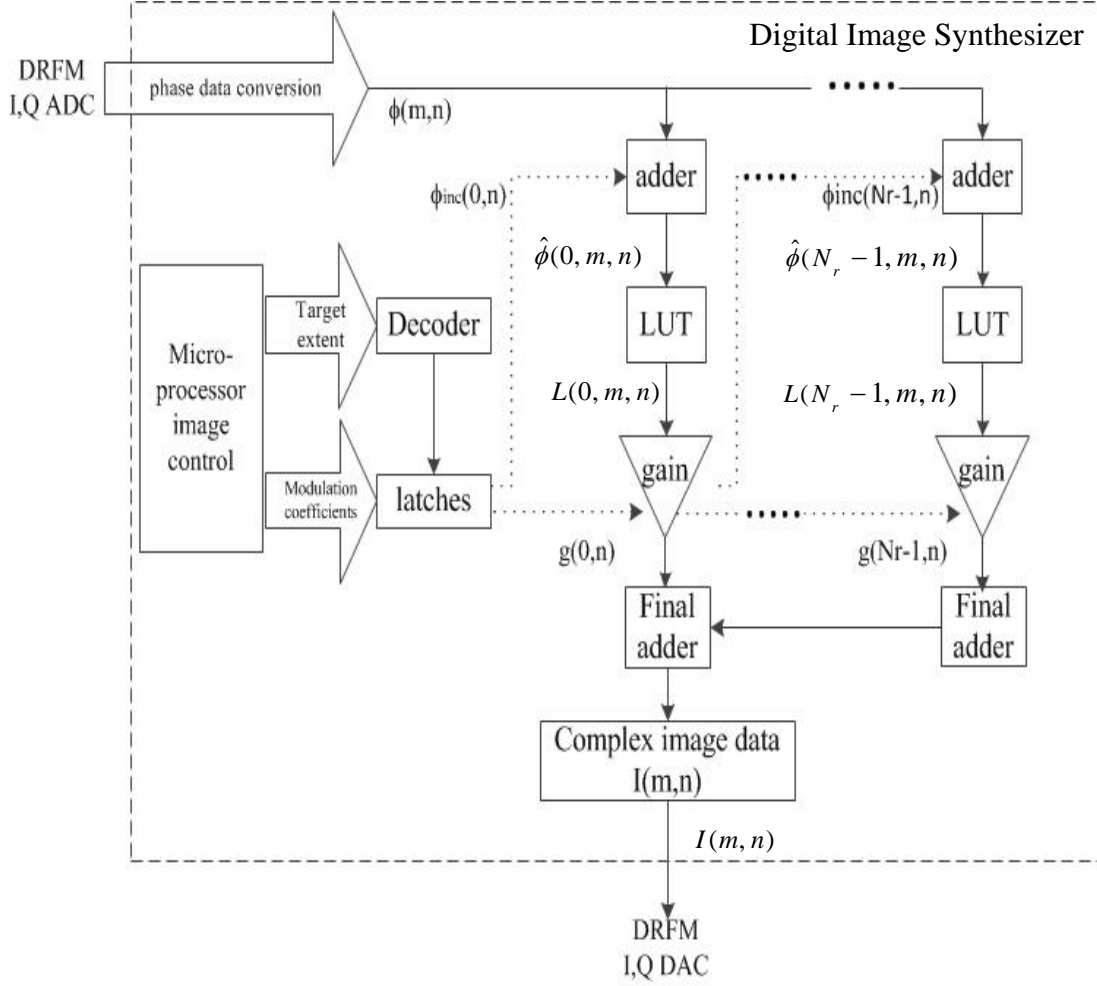


Figure 5. DIS Block Diagram (From [1]).

The following description explains the signal processing of the DIS architecture throughout this chapter and is theoretically and mathematically based on the discussion contained in references [1] and [16].

2. Digital RF Memory Phase Samples

Most of the advanced military radars process signals coherently to preserve the phase of the detected signal against the deceptive repeater jammer. The old-fashioned non-coherent jamming device is less effective and the need to replace these with newer coherent jammer techniques increases. DRFM-based jammers that store and replicate the intercepted radar signal coherently are one of the recent methods used to break through

the coherent processing of radar and maintain a reliable jamming effect. Figure 6 represents the block diagram explaining the flow of the DRFM signal processing, which is described in the following paragraphs [9].

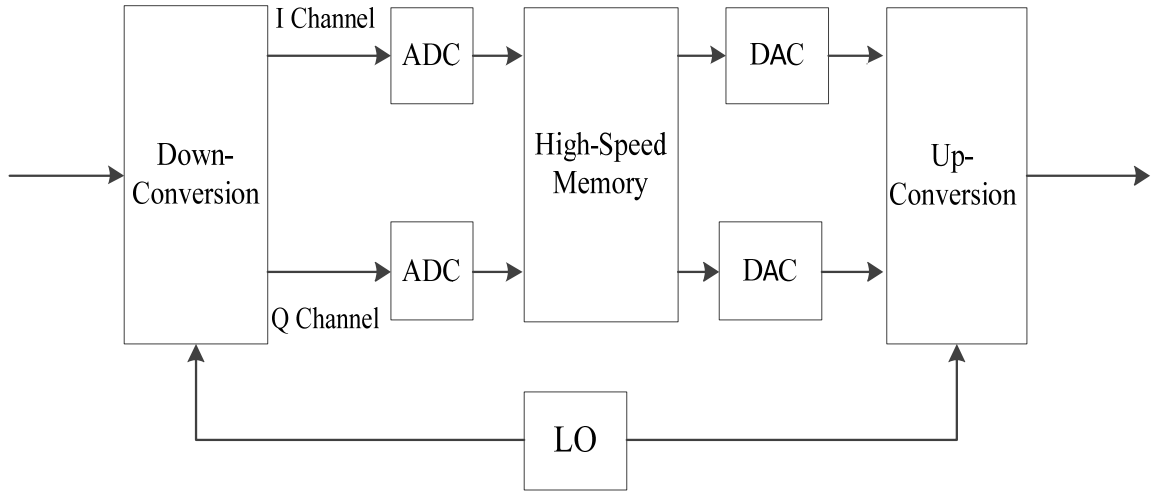


Figure 6. Functional Diagram of DRFM.

The typical DRFM process includes the following steps: (1) down-converting the frequency of the intercepted signal to intermediate frequency (IF) with a reference local oscillator (LO) and decomposing it into the in-phase (I) and quadrature (Q) components, (2) sampling and digitizing using an analog-to-digital (ADC) converter, (3) storing the sampled pulse information into the memory for generating the jamming signal purpose, (4) reconstituting the I and Q components modified with the jamming signal to analog form through a digital-to-analog (DAC) converter, and (5) up-converting the jamming signal with the original LO [6,8,13].

Among the processes mentioned above, the conversion of signals into a digital bit stream is limited by the speed of the ADC; as a result, it is necessary to choose an IF that matches the converter sampling rate. Also, the two oscillators must be very stable so that the phase information of the signal is preserved. The signal samples stored in the memory

can be utilized for various electronic counter-measure applications, including the generation of noise, synthesis of a different in-band frequency, and modulation of false targets.

For example, considering a LFM ISAR that transmits an up-chirp pulse, the complex envelope of the transmitted signal can be represented as

$$s(t) = \text{rect}\left(\frac{t}{\tau}\right) e^{j\pi\Delta t^2/\tau} \quad (3.1)$$

and that of the pulse intercepted by DRFM is

$$s_i = \text{rect}\left(\frac{t}{\tau}\right) e^{j2\pi(f_d t + \Delta t^2/2\tau)} \quad (3.2)$$

where $\text{rect}(t/\tau)$ is the rectangular function, τ is the uncompressed pulse width in seconds, Δ is the modulation bandwidth in Hertz, f_d is the Doppler frequency due to the closing rate between the ISAR and the platform with the DRFM. Notice that, in (3.2), f_d is usually in tens of Hertz and can be ignored if compared to Δ , which is in megahertz (MHz). Thus, it is reasonable to assume that the phase change within the chirp pulse is constant and (3.2) can be replaced with (3.1).

Depending on the type of DRFM used, the signal expressed in (3.1) can be phase-sampled or amplitude-sampled at a sampling time given by

$$t = \frac{m}{f_s} + n \cdot PRI \quad (3.3)$$

where m is the index of the intrapulse samples, n is the index of pulse number, f_s is the ADC sampling frequency, and PRI is the ISAR pulse repetition interval (PRI) in seconds. Although many imaging radars use variable PRI, the PRI must stay constant within the time to construct one image. Substituting (3.3) for the sampling time, t , in (3.1), the sampled phase of the DRFM intercepted signal can be expressed as

$$\phi_0(m, n) = \frac{\pi\Delta}{\tau} \left(\frac{m}{f_s} + n \cdot PRI \right)^2 \quad (3.4)$$

In the case of a k_p -bit phase-sampling DRFM, the phase information in (3.4) is generated with k_p -bit resolution by 2^{k_p} integers ranging from 0 to $2^{k_p} - 1$. Thus, after the DRFM sampling processing, the phase information expressed in (3.4) is stored in the memory in the following form

$$\phi(m, n) = \left\lfloor \frac{\phi_0(m, n)}{2\pi / 2^{k_p}} \right\rfloor \quad (3.5)$$

where $\lfloor x \rfloor$ represents the greatest integer smaller than or equal to x . The resulting phase information is then inserted into the DIS process. The identical concept of quantization is also applied to a k_q -bit amplitude-sampling the DRFM. However, it is necessary to convert the k_q -bit amplitude samples into phase before they are inserted into the DIS process as shown in Figure 6 [5,16].

3. False-Target Image Profile

In order to synthesize the false-target image with the phase and amplitude information input from DRFM (both the I and Q channels), appropriate modulations must be performed at each range cell to emulate the Doppler shift due to target rotation and the expected radar cross-section value of the reflective surface at each location in the range-Doppler plane. It is the microprocessor block in Figure 5 where a false-target image profile and the corresponding phase and gain coefficients used to synthesize the false-target image are generated.

A false-target profile is constructed by creating an N_r by N_d matrix of scattering elements, where N_r is the number of the resolution cells in range and N_d is the number of Doppler resolution cells in cross-range. An example of false-target profile for a ship is shown in Figure 7.

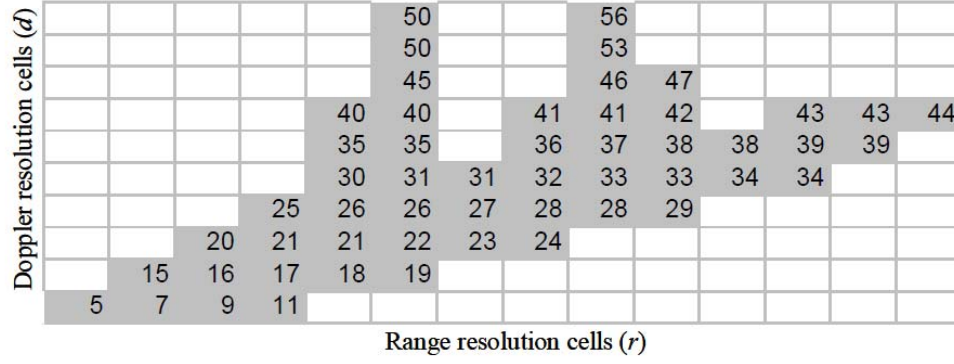


Figure 7. Range-Doppler Profile Template for A False Target.

For each (r, d) cell in Figure 7, its amplitude, $A(r, d)$, depends on the radar RCS of the scatterer contained within the cell and according to the radar equation, this RCS value is related to the distance between the ISAR and the scatterer, R , in the following form

$$R \propto RCS^{\frac{1}{4}} \quad (3.6)$$

The phase of the scatterer within each (r, d) cell, on the other hand, depends on the Doppler shift, $f(r, d)$, due to the relative angular rotation of the scatterer along the LOS of the false-target motion. Both $A(r, d)$ and $f(r, d)$ are varied on a pulse-to-pulse basis. Therefore, each cell in the profile can be expressed in a tri-dimensional matrix comprised of range cell, Doppler cell, and the number of pulses, as follows

$$T(r, d, n) = A(r, d)e^{-j2\pi f(r, d)nPRI} \quad (3.7)$$

where n is the index of pulse number. Furthermore, the signal of the false-target profile for each pulse at each range cell, r , can be obtained by summing all Doppler components within each r and is expressed as follows

$$T'(r, n) = \sum_{d=1}^{Nd(r)} T(r, d, n) \quad (3.8)$$

The phase of each false-target return is calculated as

$$\phi_T(r, n) = \text{angle}(\text{real}\{T'(r, n)\}, \text{imag}\{T'(r, n)\}) \quad (3.9)$$

where the *angle* function is equivalent to taking *arctan* function on the division of the imaginary and real components of $T'(r, n)$. Once the false-target return and its corresponding phase are determined, the DIS phase and gain coefficients, $\phi'_{inc}(r, n)$ and $g(r, n)$, are independently generated for each range cell.

The phase coefficient must be properly generated so that it is recognized by the ISAR as a successive phase variation on a pulse-by-pulse basis. Hence, for pulses after the first one ($n \neq 0$), the modified phase coefficient for the range cell r , $\phi'_{inc}(r, n)$, is obtained by subtracting the phase calculated for the current pulse from the sum of the phase and the phase variation calculated for the previous pulse. The mathematical expression is written as

$$\phi'_{inc}(r, n) = \phi'_{inc}(r, n-1) + \phi_T(r, n-1) - \phi_T(r, n) \quad (3.10)$$

As to the first pulse ($n = 0$), it is assumed to remain in phase with no variation such that the modified phase coefficient for the first pulse is

$$\phi'_{inc}(r, 0) = \phi_T(r, 0) \quad (3.11)$$

The phase coefficient in (3.11) also needs to be quantized to an integer value in accordance with the k_p -bit phase-sampling DRFM. Thus, the modified phase coefficient is given by

$$\phi_{inc}(r, n) = \left\lfloor \frac{\phi'_{inc}(r, n) 2^{k_p}}{2\pi} \right\rfloor \quad (3.12)$$

The modulation of the amplitude coefficient is similar to that of the phase coefficient. There are various methods that can be used to produce the gain coefficient, $g(r, n)$, such as uniform, exponential, and log thresholds. The exponential scheme is used for the DIS design. In Figure 7, the gain block multiplies the complex signal by $2^{g(r, n)}$, where $g(r, n)$ represents the number of left-shifts applied [1,16]. Such gain

modulation is done by shifting bit locations; the use of multiplexers is eliminated for better performance. A detailed discussion on the implementation of the multiplexer is found in [16]. The first step to obtain the gain coefficient is to normalize the magnitude of $T'(r, n)$ in (3.8) so that all magnitudes have a range of values between 0 and 1

$$T'_N(r, n) = \frac{|T'(r, n)|}{\max |T'(r, n)|} \quad (3.13)$$

The normalized magnitude is then quantized into 2^{k_g} levels, where k_g represents the number of bits controlling the left shifts. Due to the hardware limitation, some bit values may produce the same amount of shift, which results in fewer control codes available than 2^{k_g} . For instance, a gain shifter with a 4-bit control produces only 11 unique shifts instead of 16. Table 1 shows the possible quantization for the gain shifter implemented with a 4-bit control.

| Normalized Magnitude | Gain Coefficient $g(r, n)$ | Effective Gain $2^{g(r, n)}$ |
|----------------------|----------------------------|------------------------------|
| 0.8-1.0 | 10 | 1024 |
| 0.4-0.8 | 9 | 512 |
| 0.2-0.4 | 8 | 256 |
| 0.1-0.2 | 7 | 126 |
| 0.05-0.1 | 6 | 64 |
| 0.025-0.05 | 5 | 32 |
| 0.0125-0.025 | 4 | 16 |
| 0.00625-0.0125 | 3 | 8 |
| 0.0032-0.00625 | 2 | 4 |
| 0.0016-0.00625 | 1 | 2 |
| 0-0.0016 | 0 | 1 |

Table 1. Gain Modulation Quantization Table (From [5]).

4. The DIS Signal Processing

As shown in Figure 6, the DIS processes the k_p -bit phase samples in both the I and Q channels from a phase-sampling DRFM and uses a high-performance microprocessor for false-target image control. Each of the DRFM sampled phases $\phi(m, n)$, as shown in (3.5), is entered in parallel to N_r range bin modulators that are derived from the N_r range resolution cells of the false-target profile generated by the microprocessor. Along with the phase and gain coefficients, every $\phi(m, n)$ is processed through a phase adder, a look-up table (LUT), a gain block, and a summation adder within each range bin modulator.

From Figure 5, the DRFM sampled phase is first added to the phase coefficient $\phi_{inc}(r, n)$ through the phase adder and the resultant output is given as

$$\hat{\phi}(r, m, n) = \phi(m, n) + \phi_{inc}(r, n) \quad (3.14)$$

which implies the phase of the m^{th} sample of the n^{th} pulse is added with the phase coefficient at the r^{th} range cell of the same pulse.

The k_p -bit phase adder output $\hat{\phi}(r, m, n)$ is used by the LUT to index a sine and cosine value to construct a complex signal of unit amplitude with I and Q components, respectively. Thus, the LUT output is

$$L(r, m, n) = \cos(\hat{\phi}(r, m, n)) + j \sin(\hat{\phi}(r, m, n)) \quad (3.15)$$

where each of the I (cosine) and Q (sine) output channels has amplitude values ranging from -1 to 1.

The LUT output (both I and Q channels) are then amplitude modulated at the gain block in each range cell modulator. The effective gain derived from the gain coefficient on which a power of two's function is applied is referred to as the modified RCS for the false-target image that is going to be returned to ISAR. The gain modulated channels can be expressed as

$$S(r, m, n) = 2^{g(r, n)} L(r, m, n) = 2^{g(r, n)} e^{j(\phi(m, n) + \hat{\phi}_{inc}(r, n))} \quad (3.16)$$

Following the gain modulation, all further range cell processors are summed with the current processor and passed forward. The final adder block within each range cell modulator sums the result after amplitude modulation with its adjacent (delayed) adder output and sends the result forward to the adder in the next modulator. The final complex output pulse is collected at the adder in the first range cell modulator. In other words, each output pulse is the superposition of copies of the pulse, each delayed with respect to one another by the adder delay, scaled differently by the gains and phase rotated by as

$$\begin{aligned} I(m, n) = & 2^{g(0, n)} e^{j(\phi(m, n) + \phi_{inc}(0, n))} \\ & + z^{-1} \left[2^{g(1, n)} e^{j(\phi(m, n) + \phi_{inc}(1, n))} \right] \\ & + z^{-2} \left[2^{g(2, n)} e^{j(\phi(m, n) + \phi_{inc}(2, n))} \right] + \dots \\ & + z^{-(N_r-1)} \left[2^{g(N_r-1, n)} e^{j(\phi(m, n) + \phi_{inc}(N_r-1, n))} \right] \end{aligned} \quad (3.17)$$

where z^{-1} represents the delay inherent in each adder[1].

For simplicity, the final output of the DIS false-target image signal for the m^{th} sample of the n^{th} pulse is rewritten as

$$I(m, n) = \sum_{r=0}^{N_r-1} S(r, m, n) = \sum_{r=0}^{N_r-1} 2^{g(r, n)} e^{j(\phi(m-r, n) + \phi_{inc}(r, n))} \quad (3.18)$$

Finally, the digitized DIS output signal is passed to a DAC and transformed into an analog signal. The same LO used during the ISAR signal reception phase is further applied to up-convert the output signals onto the ISAR carrier frequency. The final up-converted jamming signal is then retransmitted back to the ISAR for image processing, which is discussed in Chapter II.

5 Variant of the DIS Design with Multiple False Targets

Several efforts have been devoted to improving the DIS design since it was first proposed. In addition to improving the software codes, algorithms for the reduction in response time, and a better performance in parallel processing operations, other efforts have further modified the phase coefficient so that the original DIS design is able to

generate multiple false targets. In [17], an algorithm that generates multiple false targets is proposed, and an example of the resulting ISAR image is shown in Figure 8.

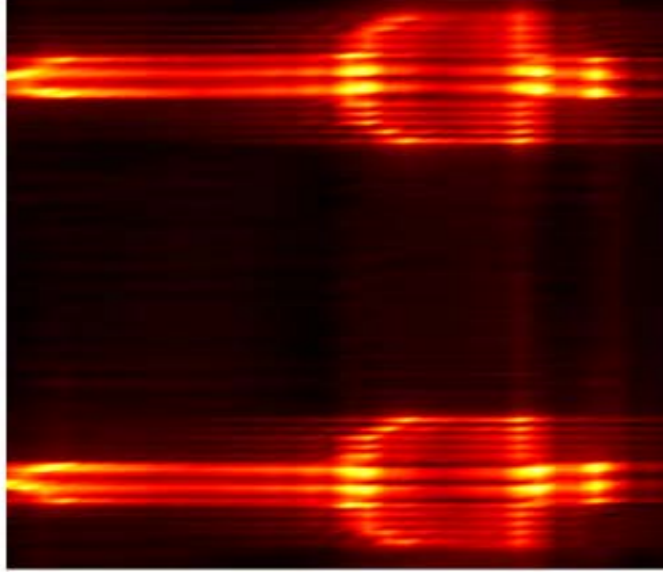


Figure 8. ISAR Image with Multiple False Targets (From [17]).

In order to accommodate the original DIS design to generate the effect of multiple false targets on the ISAR image, it is the phase of the false-target return at each range cell, $\phi_T(r, n)$, in (3.9) that must be modified as [17]

$$\phi_{T_mod}(r, n) = k_m \phi_T(r, n) \quad (3.19)$$

where ϕ_{T_mod} is the modified phase and k_m is a phase modulator with the following form

$$k_m = (-1)^r \quad (3.20)$$

The phase increment in (3.10) becomes

$$\phi'_{inc}(r, n) = \phi'_{inc}(r, n-1) + \phi_{T_mod}(r, n-1) - \phi_{T_mod}(r, n) \quad (3.21)$$

From (3.20), it is clear that the phase modulator reverses the phase by 180 degrees at each of the odd range cells. In other words, half of the range cells in the false-target profile have opposite phase values while those of the other half remain unchanged.

Compared to (3.17), the final false-target signal becomes [17]

$$\begin{aligned}
I(m, n) &= \sum_{r=1}^{N_r} 2^{g(r, n)} e^{j(\phi(m, n) + \phi_{mc}(r, n))} \\
&= e^{j\phi(m, n)} \sum_{r=1}^{N_r/2} 2^{g(2r, n)} e^{j\phi_{mc}(2r, n)} + e^{j\phi(m, n)} \sum_{r=1}^{N_r/2} 2^{g(2r-1, n)} e^{-j\phi_{mc}(2r-1, n)}
\end{aligned} \tag{3.22}$$

where two identical false targets are generated. The image containing the term $e^{j\phi_{mc}(2r, n)}$ is attributed from the even-range cells of the false-target profile and the other with the term $e^{-j\phi_{mc}(2r-1, n)}$ is from the odd-range cells.

C. CHAPTER SUMMERY

A discussion of the electronic attack measures against ISAR, both the noise and deception jamming, is provided in the beginning of this chapter. Next, the DIS concept is mathematically introduced, including the signal processing at the DRFM, the generation of false-target profiles and the final false-target signal. Finally, a multi-false-targets jamming technique, modified from the DIS design, is presented, and the difference between the original and new DIS algorithms is described mathematically.

In the next chapter, the EP techniques that can be used by the ISAR to protect itself from deception EA are described.

THIS PAGE INTENTIONALLY LEFT BLANK

IV. METHODS TO DISCRIMINATE FALSE TARGETS

As mentioned in Chapter III, jammers that use DRFM-based DIS false targets are considered an effective scheme to confuse SAR or ISAR for target image acquisition. As a result, the capability of recognizing whether an imaged target is real becomes more and more critical for radar reliability.

There are several methods or algorithms developed to discriminate false targets from real targets and to filter them out from the operator's view. Methods that have been investigated include those based on the target's continuity, pulse diversity, and cross-track interferometry which represent the three general schemes that have been described.

A. CONTINUITY OF THE FALSE TARGET IN THE ISAR IMAGE

The recognition of a DIS false target can be performed by inspecting the continuity of the target within the ISAR image. An example is shown in Figure 9. Figure 9a is the image of ship taken by the AN/APS-137 ISAR radar, while Figure 9b is the one obtained from the simulation of the DIS false-target based on the size and shape of the same ship.

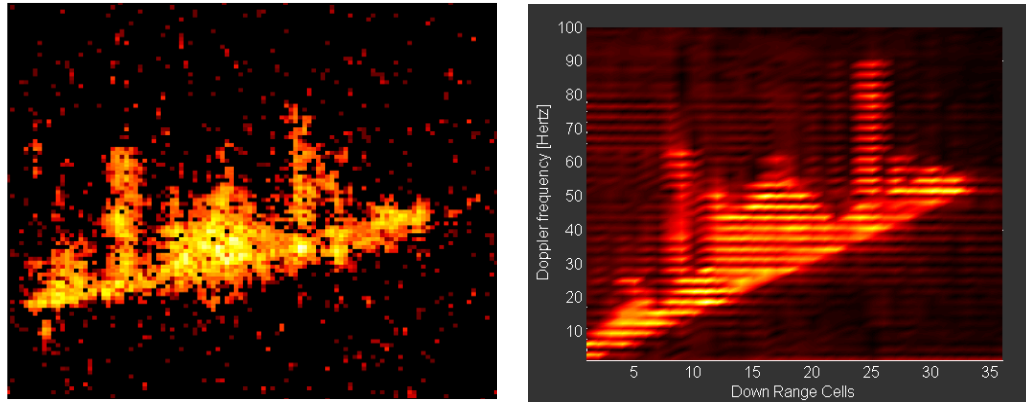


Figure 9. Comparison of ISAR Images on Real Target and DIS False Target.

In both images, the superstructure of the ship can be identified and the size of the ship can be approximately estimated but it is not difficult to distinguish the real target from the decoy. Due to the complex reflectivity of the target's surface and the Doppler

shift caused by the background clutter, the ISAR imaging processing cannot perfectly compensate for the target's motion in range and cross-range dimensions [4]. Hence, the ISAR image of a real target in Figure 9a is blurred, especially at the edge of the surface. Also, the image of the ship's superstructure is continuous in both range and cross-range domains, which means there is a correlation in Doppler shift between consecutive reflective surfaces.

The simulation of the ISAR image for the DIS false-target in Figure 9b, on the other hand, is discontinuous in both dimensions. Such discontinuity of the DIS false-target image is fundamentally derived from the design of the false-target profile in the DIS processing.

For the DIS false-target profile in Figure 8, the Doppler shift assigned for each surface of the false target within a range cell is identical on a pulse-to-pulse basis. In other words, for a range cell along the radar LOS, every reflective surface is assumed to have the same Doppler shift on each pulse. This assumption implies that there is no correlation between consecutive reflective surfaces and results in a gap in the cross-range domain among all range cells. The discontinuity in Doppler occurs during the ISAR cross-range compression process.

Another reason the DIS false target is discontinuous is the digitization of the phase information in order to meet the DRFM architecture. This digitizing process actually transforms the phase information into an integer representation, which causes a gap, or an error, between two consecutive cross-range cells at each range cell. Therefore, the discontinuity in cross-range is produced after the ISAR cross-range compression process is performed [4].

Other than taking advantage of the deficiency of the DIS design to determine the continuity of the image, altering the ISAR's Doppler resolution can also be an option that enlarges the discontinuity of the target image and helps in identifying the false target. Figure 10 shows simulation results of an ISAR image in three different radar Doppler

resolutions. These simulations are based on the same DIS false-target profile and can be used as an example to illustrate the relationship between radar Doppler resolution and the discontinuity of false-target images.

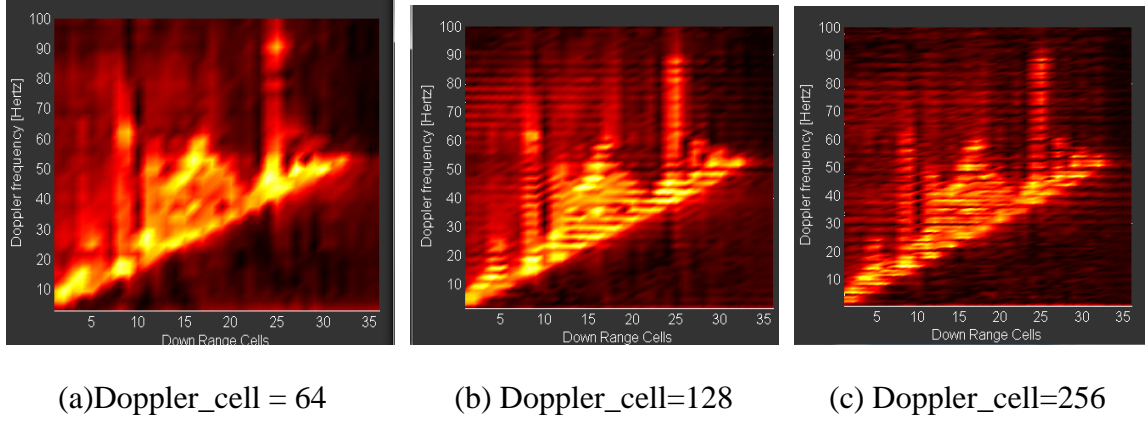


Figure 10. Simulations on ISAR False Target with Different Doppler Resolutions.

From Figure 10a, 10b, and 10c, it is obvious that the finer the Doppler resolution, or the more the Doppler resolution cells, the easier to pick up the gap between two consecutive cross-range cells. Thus, an experienced radar operator can examine the continuity of a target image and determine the authenticity of the target by changing the radar Doppler resolution.

To sum up, the method for ISAR to discriminate DIS false targets by examining the continuity of the false-target image is probably one of the most economical methods that focus on the flaw of the DIS design. The DIS design requires a modification to defeat such EP operations.

B. PULSE DIVERSITY WITH A DRFM PENALIZING ALGORITHM

The strategy that discriminates the false target using pulse diversity was originally proposed to enhance the performance of SAR against the DRFM-based jammer. It is possible to deploy this technique on ISAR to neutralize the DRFM-based jamming signal that contains the DIS false-target signal; though few efforts have been devoted in this area. Since the pulse diversity method is developed for SAR, the following description will be presented from the SAR point of view.

Aperture radars utilizing the pulse diversity method are involved in an alternation of the transmitted signal and/or its parameters in the fast-time domain at each PRI [18]. In most of the cases, a random phase is added onto each of the radar pulses initially, on a pulse-to-pulse basis before transmission. Such initial phase information is kept within the radar where the DRFM-based jammer has no access. When the DRFM jamming signal based on the previous pulse arrives at the radar receiver, its phase information does not match with that of the current radar pulse and is mostly likely to be filtered by a matched filter. As a result, the radar becomes more resistant against a DRFM-based jammer. A DRFM penalizing algorithm is further proposed in [19] and [20] to enhance the pulse diversity method. The DRFM penalizing algorithm is a two-dimensional, range-Doppler signal processing that effectively negates the DRFM-based jammer image. A system block diagram illustrating the process for both the pulse diversity and the DRFM penalization is shown in Figure 11.

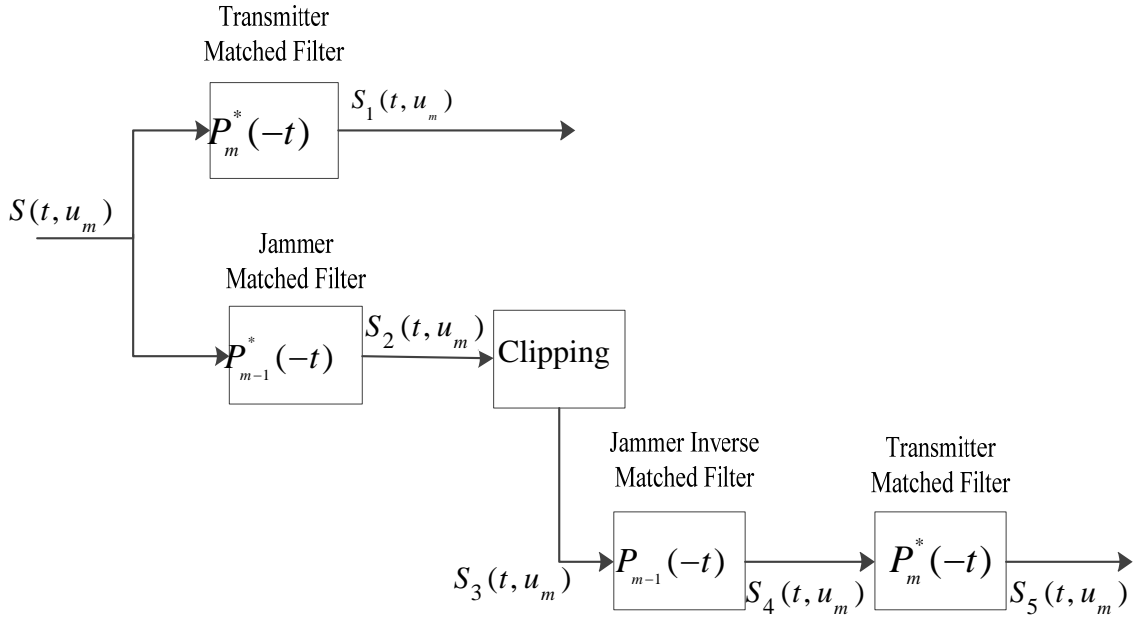


Figure 11. Block Diagram for Radar's DRFM Penalization in Range Process.

In Figure 11, the signal received by the radar is first processed in sequence through a set of matched filters, including the transmitter matched filter and jammer matched filter. In order to construct the jammer matched filter, some characteristics of the jammer, like its transmitting pulse sequence, must be known beforehand.

Consider a SAR system with the following pulse sequence

$$P_m(t), \quad m = 1, \dots \quad (4.1)$$

where m is the index identifying the discrete measurement in the radar slow-time domain, u , and t represents the time index in the radar fast-time domain. The corresponding jammer pulse sequence is assumed to be

$$P_{m-1}(t), \quad m = 1, \dots \quad (4.2)$$

Thus, the signal received by the radar at m^{th} aperture position can be expressed as [20]

$$S(t, u_m) = S_{ACT}(t, u_m) + S_J(t, u_m) \quad (4.3)$$

where $S_{ACT}(t, u_m)$ represents the signal returned from the actual target, and $S_J(t, u_m)$ represents the DRFM false-target signal. Upon reception, $S(t, u_m)$ is down-converted to base band and applied to the transmitter and jammer matched filter, respectively, where $S_1(t, u_m)$ and $S_2(t, u_m)$ are outputs generated.

The received signal is match filtered with the m^{th} pulse to reduce the effect of the jammer signal, and $S_1(t, u_m)$ is generated as follows

$$\begin{aligned} S_1(t, u_m) &= S(t, u_m) * P_m^*(-t) \\ &= S_{ACT}(t, u_m) * P_m^*(-t) + S_J(t, u_m) * P_m^*(-t) \end{aligned} \quad (4.4)$$

Since $S_J(t, u_m)$ is the signal based on the information of the previous pulse, which differs with the current pulse in phase, the jammer effect within $S_1(t, u_m)$ is weakened. An example picture of the resultant $S_1(t, u_m)$ from [19] is shown in Figure 12, in which the strength of the jammer signal is found to be approximately 20 dB lower than that of the real target return. Such result can be further considered as the effect of deploying pulse diversity in phase against the DRFM false-target jamming.

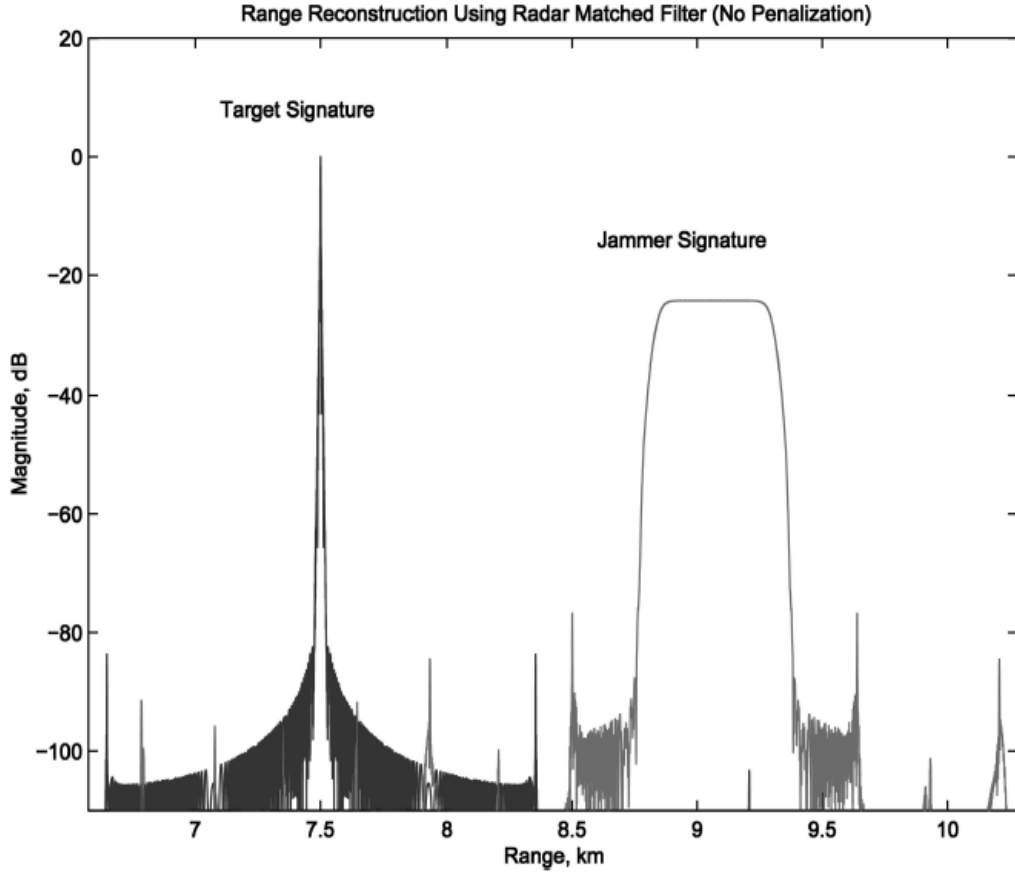


Figure 12. Radar Matched Filtered Signal $S_1(t, u_m)$ (From [19]).

The received signal is also applied to the jammer matched filter that is based on the previous pulse and generates an output, $S_2(t, u_m)$, with the following expression

$$\begin{aligned} S_2(t, u_m) &= S(t, u_m) * P_{m-1}^*(-t) \\ &= S_{ACT}(t, u_m) * P_{m-1}^*(-t) + S_J(t, u_m) * P_{m-1}^*(-t) \end{aligned} \quad (4.5)$$

By the same token, the real target return signal, $S_{ACT}(t, u_m)$, is weakened due to the mismatched phase between the current and previous pulses. An example picture of the resultant $S_2(t, u_m)$ from [19] is shown in Figure 13.

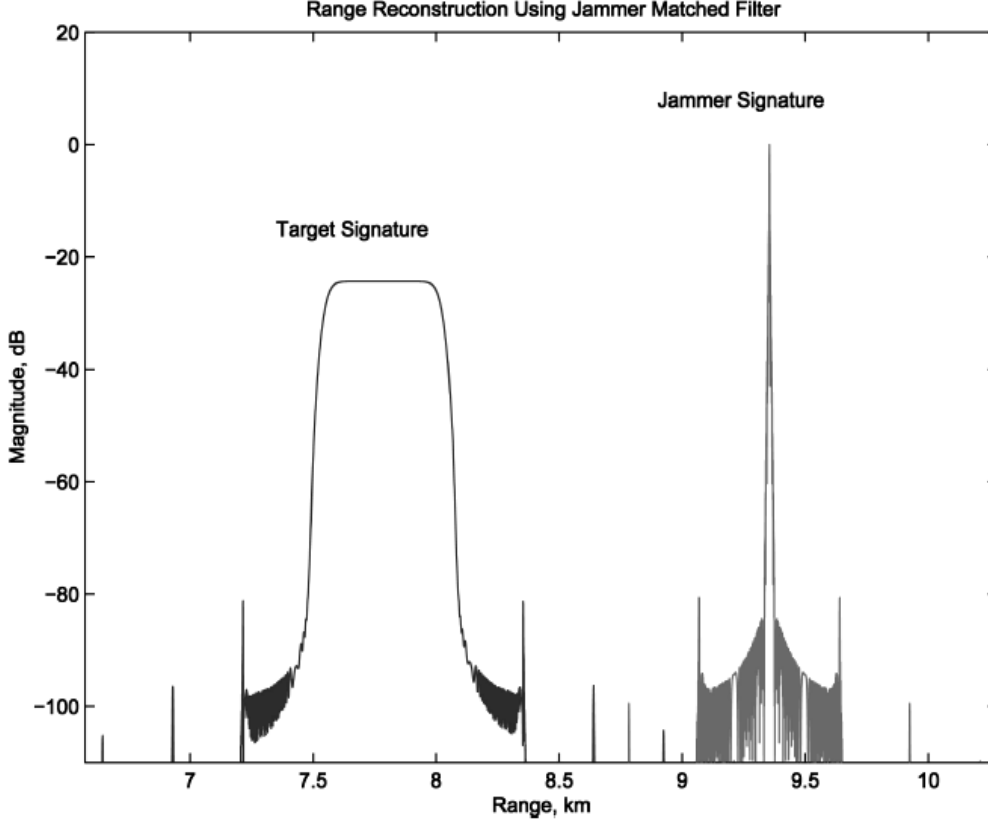


Figure 13. Jammer Matched Filtered Signal $S_2(t, u_m)$ (From [19]).

A hard-limit (threshold) of -20 dB is applied onto $S_2(t, u_m)$ to chop off the peaks of the jammer signal, and the threshold output is denoted as $S_3(t, u_m)$. The hard-limited data is then transformed with a jammer inverse matched filter with the jammer pulse sequence so that the final signal, $S_5(t, u_m)$, contains the information only on the real target. The mathematical expressions are

$$S_4(t, u_m) = S_3(t, u_m) * P_{m-1}(t) \quad (4.6)$$

$$S_5(t, u_m) = S_4(t, u_m) * P_m^*(-t) \quad (4.7)$$

An example picture of the resultant $S_5(t, u_m)$ is shown in Figure 14. The strength of the jammer signal is found to be approximately 40 dB less than that of the real target return. Although the algorithm can be further performed in azimuth domain for better

performance, as described in [20], the example in Figure 14 suggests DRFM penalizing algorithm in suppression of the DRFM false-target jamming.

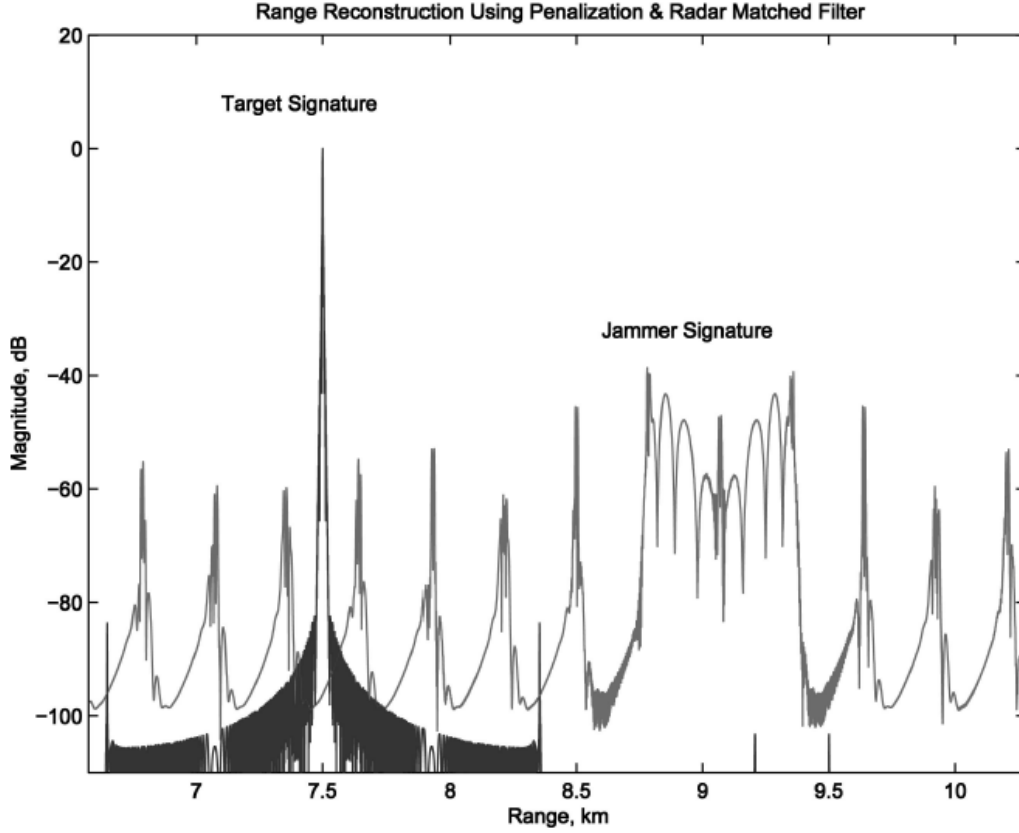


Figure 14. Jammer-Penalized Output Signal $S_5(t, u_m)$ (From [19]).

C. CROSS-TRACK INTERFEROMETRY

The dual-aperture antenna cross-track interferometer is a method, separate from those discussed above, that is proposed to locate the false target generated by the deceptive jammer. This method utilizes the phase information of the image, pixel-by-pixel, and a spatial cancellation algorithm to separate false targets from real targets. Figure 15 shows a flow diagram of the dual-aperture cross-track interferometry scheme, in which it is easy to identify that the spatial cancellation is performed after the synthetic image is generated. Since this method does not involve complicated signal processing, it has great possibility to be applied on ISAR for the DIS false-target recognition, although it was originally proposed for SAR.

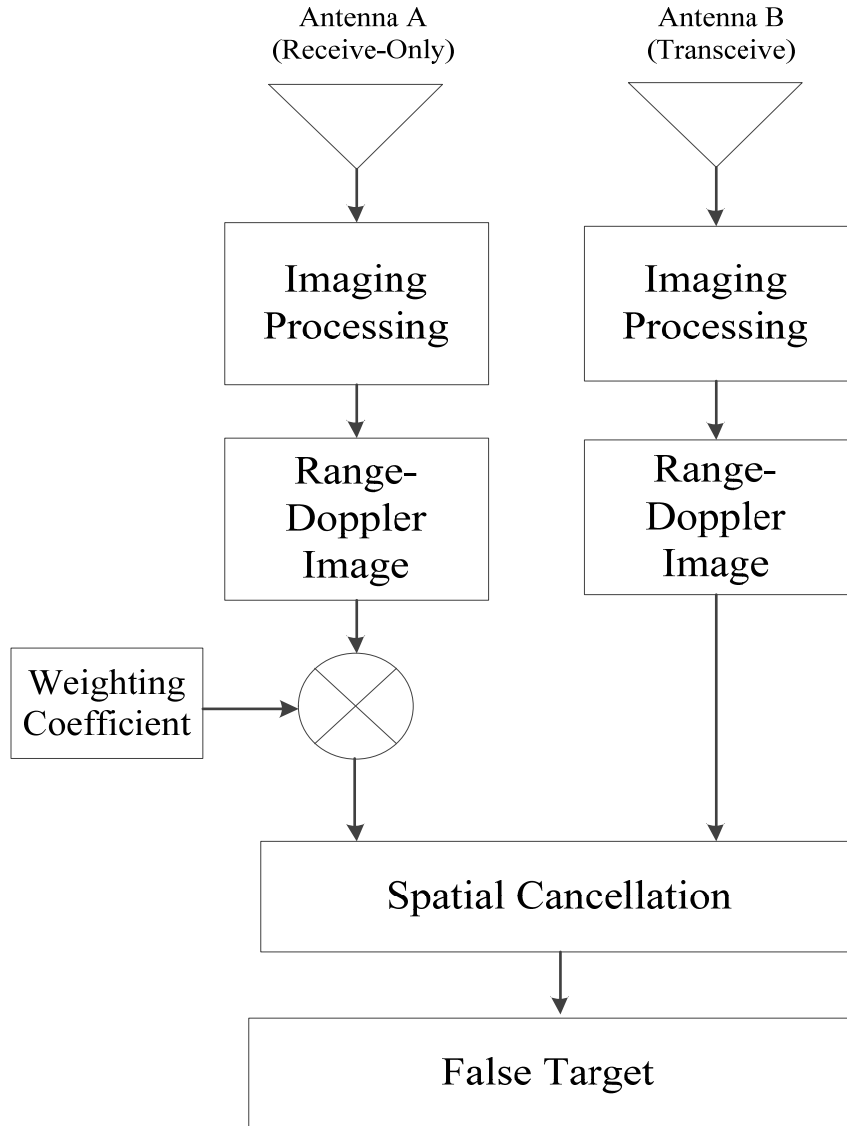


Figure 15. Flow Diagram of the Dual-Aperture Cross-Track Interferometry Scheme.

To execute the cross-track interferometry method, two identical aperture antennas, SAR A and SAR B, must be aligned in parallel with a fixed displacement, d . The geometry of the dual-aperture antenna is shown in Figure 16.

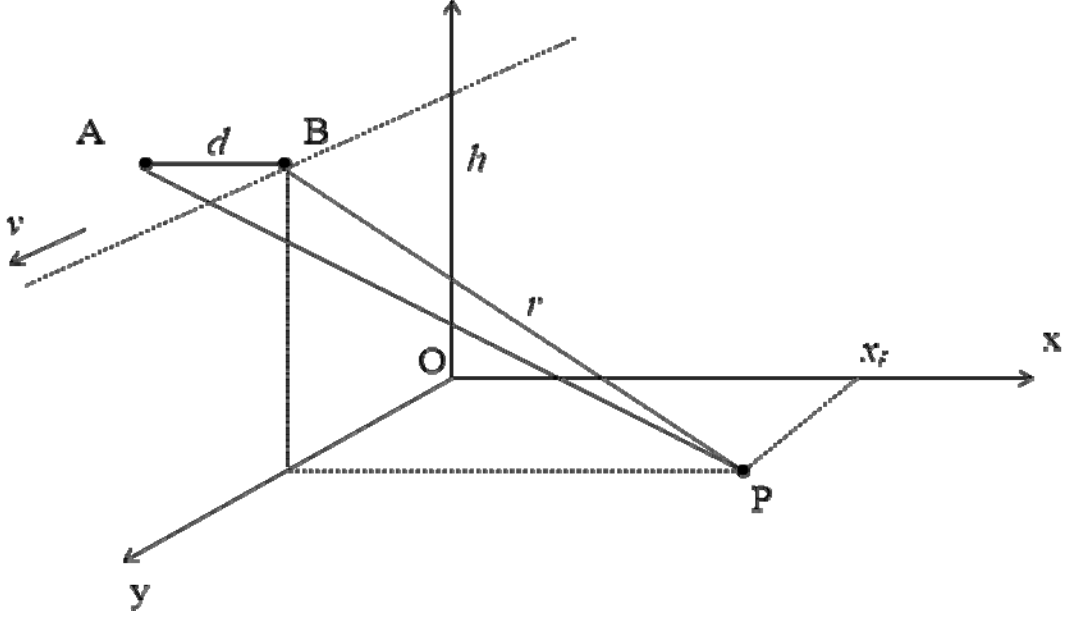


Figure 16. Geometry of the Dual-Aperture Antenna Cross-Track Interferometry (from [15]).

SAR B operates in transceive mode, while SAR A is in a receive-only mode. Therefore, two synthetic images are obtained after the processing, namely image A and image B, respectively. Consider that a reflective surface, or a scatterer, is shown at location P on both images, and the slant range between SAR B and P is represented by r . There is a phase value with respect to the scatterer at P for both images, and the difference between those two phase values is [14]

$$\psi_{AB} = \psi_A - \psi_B = \frac{2\pi}{\lambda r} (\overline{AP} - \overline{BP}) \approx \frac{2\pi}{\lambda r} (d^2 - 2dx_p) \quad (4.8)$$

where x_p is the x-axis coordinate of P and λ is the wavelength of the antenna radiation.

Assume a false target is generated by a platform with a DRFM jammer located at P, and the x-axis coordinate of the false target is denoted as x'_p . Thus, according to (4.8), the phase difference at which the false target is located between two images can be expressed as

$$\psi'_{AB} = \psi'_A - \psi'_B \approx \frac{2\pi}{\lambda r'}(d^2 - 2dx'_p) \quad (4.9)$$

where r' is the slant range between SAR B and the false target location. For simplicity, the false target is assumed to be in an extend such that $r \approx r'$. Then, (4.9) can be rewritten as

$$\psi'_{AB} = \psi'_A - \psi'_B \approx \frac{2\pi}{\lambda r}(d^2 - 2dx'_p) \quad (4.10)$$

A weighting coefficient, w_{mn} , is chosen to have the value of $e^{-j\psi_{AB}}$, which is related to x_p . This weighting coefficient is applied to the imaging output of SAR A, so that the normalized signal of each image pixel on image A can be expressed as

$$S_A = S_A e^{-j\psi_{AB}} = e^{j\psi_A} e^{-j\psi_{AB}} \quad (4.11)$$

while the normalized signal of the same image pixel on image B can be expressed as

$$S_B = e^{j\psi_B} \quad (4.12)$$

The spatial cancellation block in Figure 15 essentially calculates the difference of the signal of the same location pixel between both images. The output of the spatial cancellation block is

$$S_{AB} = S_A e^{-j\psi_{AB}} - S_B = e^{j\psi_A} e^{-j\psi_{AB}} - e^{j\psi_B} \quad (4.13)$$

Thus, if there is no false target and the image pixel, P , contains only the real target, the spatial cancelation output is

$$\begin{aligned} S_{AB} &= S_A e^{-j\psi_{AB}} - S_B \\ &= e^{j\psi_A} e^{-j(\psi_A - \psi_B)} - e^{j\psi_B} \\ &= e^{j\psi_B} - e^{j\psi_B} = 0 \end{aligned} \quad (4.14)$$

If, on the other hand, the same image pixel contains both the real and false-target returns, the spatial cancelation becomes

$$\begin{aligned}
S_{AB} &= (S_A + S'_A)e^{-j\psi_{AB}} - (S_B + S'_B) \\
&= (e^{j\psi_A} + e^{j\psi'_A})e^{-j(\psi_A - \psi_B)} - (e^{j\psi_B} + e^{j\psi'_B}) \\
&= e^{j\psi_B} \left[e^{j(\psi_B - \psi_A + \psi'_A - \psi'_B)} - 1 \right] \\
&= e^{j\psi_B} \left[e^{j\left(\frac{2\pi d}{\lambda r}(x'_p - x_p)\right)} - 1 \right] = 0
\end{aligned} \tag{4.15}$$

for the case $x'_p = x_p$. Thus, from (4.14) and (4.15), it can be concluded that under two circumstances the output of the spatial cancelation on a pixel of an image is cancelled. Either there is no false target, or there is a false target and such false target lies on top of the real target within the same pixel of the synthetic image. In both cases, the image originally shown in the pixel is filtered.

There is one condition left for discussion, i.e., a false target that lies at a certain extent from the jammer platform, or the real target. In this case, $x_p \neq x'_p$, and the output of the spatial cancellation is not 0. As a result, the signal of the real target is filtered while that of the false target remains on the image. After the completion of the process for every pixel on the image, the false target is portrayed and analyzed. The filtered real target is not completely lost; rather, it remains on the output image after the cancellation but at a weaker energy level, due to the inherent calculation errors in phase throughout the synthetic imaging processing.

D. CHAPTER SUMMERY

Different strategies have been considered to recognize, or even defeat, the false-target signal generated by the DIS on a DRFM platform. Three different methods based on the continuity of the target image, pulse diversity, and cross-track interferometry, respectively, are described in this chapter. The fundamental theory and mathematical expressions are also included within each individual discussion.

Among these three methods, the methods based on the pulse diversity and cross-track interferometry are designed to reject the DRFM-based jammer either before the image compression processing or after the range-Doppler image is generated. In other

words, there is no better way for current DIS design to generate the false-target image on radars capable of these two EP strategies.

Discriminating the DIS false target through determining the continuity of the target image is a method that takes advantage of the deficiency of the DIS design in the gap produced in cross-range domain. If a modification can be developed for the DIS design to compensate for such deficiency, which makes the DIS false-target image more continuous in cross-range domain, the false-target image will be more realistic and resistant to this discrimination method.

In the next chapter, the addition of sea clutter to the DIS model is discussed in an effort to counter the image discontinuity EP technique used by ISAR.

THIS PAGE INTENTIONALLY LEFT BLANK

V. THE DIS DESIGN WITH A SEA CLUTTER MODULE

This chapter presents a modified DIS design incorporating a new sea clutter module. The purpose of adding the sea clutter module into the DIS design is to add a sea clutter effect to the false target, so that the interaction between the reflective surface of the target object and the background clutter is emulated, which makes the false-target image more realistic. It is shown that the Doppler shift derived from the sea clutter can be used to ease the discontinuity in the cross-range domain as described in previous chapters.

The chapter starts with an introduction on theoretical methods that characterize the behavior of sea clutter, followed by an illustration on how the sea clutter module generates the sea clutter profiles using the DIS signal processing.

The MATLAB code is composed of three major files and some minor files for parameter tracking purposes. Those main files must be executed in the order of *extract_para_ship_v5*, *mathost_v5*, and *simhwchk_v5*. In *extract_para_ship_v5*, the modification coefficients for both DIS and the sea clutter module are obtained for later false-target generation. In *mathost_v5*, the DRFM samples used by DIS and the reference signal fed at the ISAR receiver are simulated. Finally, the DIS signal processing and ISAR image compression for producing a target range-Doppler image are simulated in *simhwchk_v5*. The simulation result of the modified DIS is provided and compared with that of the original DIS design.

A. INTRODUCTOIN OF SEA CLUTTER MODELING

Observations of sea clutter are normally associated with particular characteristics of the sea surface and the environment, such sea waves, clutter reflectivity, and wind speed. Because of the dependency on various complicated environmental parameters, it is not an easy task to establish a model that precisely describes the behavior of sea clutter in detail. It is not always clear which environmental parameter is the most critical, and even if determined, it is often too difficult to measure such parameters accurately through the real sea conditions.

1. Gaussian Clutter Model

A complex Gaussian process is often developed to model the sea clutter in a low-resolution maritime radar system. When the radar illuminates a collection of scatterers (or clutter), each scatterer makes a contribution to the returned field. Each of these individual scatter fields is represented in a complex form that is known as the I and Q components. Consequently, each of the complex fields can be summed up to give a resultant vector to form the total scattered field, E , as follows

$$E = \sum_{n=1}^N a_n \quad \text{and} \quad (5.1)$$

$$a_n = \sqrt{\sigma_n} e^{j\phi} \quad (5.2)$$

where a_n represents the individual scatterer, N represents the number of scatterers, σ_n is the scatterer cross section value, and ϕ represents the scatterer phase.

For a low-resolution radar system, the resolution cell is large enough to cover a large number of scatterers, which are considered as evenly distributed and decorrelated when illuminated by radar. Based on such assumptions, it is possible to develop a statistical Gaussian model, with a probability density function (pdf) for the clutter as follows [22,23]

$$P(E_I, E_Q) = \frac{1}{\pi x} \exp(-(E_I^2 + E_Q^2) / x); \quad -\infty \leq E_I, E_Q \leq \infty \quad (5.3)$$

The corresponding pdf of the envelope and intensity of the clutter signal can be expressed as

$$P(E) = \frac{2E}{x} \exp(-E^2 / x); \quad E = \sqrt{(E_I^2 + E_Q^2)}; \quad 0 \leq E \leq \infty \quad (5.4)$$

$$P(z) = \frac{1}{z} \exp(-z / x); \quad z = E^2; \quad 0 \leq z \leq \infty \quad (5.5)$$

where x is the mean intensity of the clutter return signal. The intensity can be directly linked to the received power in the radar equation in the following form

$$x = \frac{P_t G_t G_r \lambda^2 \sigma^o}{(4\pi)^3 R^4 L} \quad (5.6)$$

where P_t is the power of the signal transmitted by the radar, G_t and G_r are the gain of the radar, λ is the radar wavelength, R is the distance between the radar and the jammer, σ^o is the normalized clutter RCS, and L is the overall loss.

Notice that, in (5.2), the phase of each scatterer is assumed to be constant, and thus, the Gaussian model in (5.3) carries a uniform distribution in phase. If the phase values are different, then this leads to a non-uniform distribution in phase for the Gaussian model, and is described in [24].

2. Compound K-Distribution Model

Although the Gaussian model is reasonable to represent the behavior of the sea clutter for calculating the performance of low-resolution radar systems, the same model fails if applied to a high-resolution system, mainly due to the difference in resolution and the number of scatterers covered by a resolution cell. In a high-resolution radar, the sea surface has more resolution cells, such that some of the larger-scale structures of the sea surface can be further decomposed into several smaller structures. The decomposition makes the clutter much more variant than what is seen in low-resolution radar, i.e., the speckle-like and spike-like clutter. In this case, the assumption that supports the Gaussian model may not hold anymore, and a realistic non-Gaussian clutter model is needed.

As mentioned earlier, the structure of the sea surface is very complex. Many independent small-scale structures within a single high-resolution cell can be recognized as even-distributed speckle-like clutters and described locally by the Gaussian clutter return, as shown in (5.5). However, those structures are possibly modulated by other more slow-changing large-scale structures at the same time, which implies a need to modify the local power derived from the Gaussian model.

In order to take the dependency of the mean local power x into account, the pdf of the envelope of the clutter returns of the Gaussian model in (5.4) can be rewritten as [22]

$$P(E | x) = \frac{2E}{x} \exp(-E^2 / x); \quad 0 \leq E \leq \infty \quad (5.7)$$

Here, the mean local power itself is a random variable with a pdf $P_c(x)$. By analyzing a sufficiently large quantity of data, it is found that the gamma distribution is best fit to the measured data, and thus

$$P_c(x) = \frac{b^\nu}{\Gamma(\nu)} x^{\nu-1} \exp(-bx); \quad 0 \leq x \leq \infty \quad (5.8)$$

where the gamma distribution is described by a gamma function, $\Gamma(\bullet)$, a scale parameter, b , and a shape parameter, ν .

The pdf of the envelope of the non-Gaussian clutter is obtained by integrating the local Gaussian clutter returns with mean local power x over $P_c(x)$ [22,25]

$$\begin{aligned} P(E) &= \int_0^\infty P(E | x) P_c(x) dx \\ &= 2E \int_0^\infty \frac{1}{x} \exp(E^2 / x) P_c(x) dx \end{aligned} \quad (5.9)$$

When $P_c(x)$ is replaced by the result from (5.8), the pdf in (5.9) can be rewritten as [22]

$$\begin{aligned} P(E) &= \frac{2Eb^\nu}{\Gamma(\nu)} \int_0^\infty x^{\nu-2} \exp(-bx - E^2 / x) dx \\ &= \frac{4E^\nu b^{(\nu+1)/2}}{\Gamma(\nu)} K_{\nu-1}(2E\sqrt{b}) \end{aligned} \quad (5.10)$$

and the corresponding pdf of the intensity becomes

$$P(z) = \frac{2b^{(\nu+1)/2} z^{(\nu-1)/2}}{\Gamma(\nu)} K_{\nu-1}(2\sqrt{bz}); \quad \text{where } z = E^2 \quad (5.11)$$

where K function represents the modified Bessel function. From (5.7) to (5.9), a general model with compound pdf is defined to emulate the non-Gaussian clutter (sometimes called the K-distribution model due to the utilization of the K function).

he K-distribution model, as described, was developed by K.D. Ward to simulate sea clutters when observed by a high-resolution radar. This model suggests that the amplitude of the K-distributed clutter within a resolution cell can be generated by a combination of two statistical random numbers, the Gaussian random number and the gamma random number [22,23].

Except for the speckle-like clutter, there are events where the discrete spike-like clutter (i.e., the burst) occurs within a radar resolution cell. The K-distributed model is further modified to incorporate the spike, which results in what is known as the KA model. The corresponding pdfs for the Gaussian and gamma distributed components become [22]

$$P(z|x) = \sum_{m=0}^{\infty} \frac{1}{x + m\sigma_{sp}} \exp\left(\frac{-z}{x + m\sigma_{sp}}\right) P_m(m); \quad 0 \leq z \leq \infty \quad (5.12)$$

$$P_c(x) = \frac{b^\nu}{\Gamma(\bullet)} x^{\nu-1} \exp(-bx); \quad 0 \leq x \leq \infty \quad (5.13)$$

where σ_{sp} represents the local mean spike power, m represents the number of spikes in a resolution cell, x represents the local mean speckle power, and $P_m(m)$ represents the probability of m spikes occurring in a resolution cell based on the Poisson distribution. In this model, it is assumed that the mean number of spike-like clutter in each resolution cell is \bar{N} , and $\bar{N} \ll 1$, so that $P_m(m)$ is defined as [22]

$$P_m(0) = 1 - \bar{N}$$

$$P_m(1) = \bar{N}$$

$$P_m(m \geq 2) = 0$$

which, in other words, the probability for more than two spikes occurring within a range cell is zero.

3. Doppler Spectrum Based on K-Distributed Model

The structure of the sea surface can sometimes be complex due to the inconsistent variation of the compound component of the sea structure over an observation time interval T . Some structures may vary in less than a second while others on the order of many seconds, and different choices of T may suggest different results when analyzing the sea clutter. In practice, such T is carefully chosen to be at least as large as the time taken for the cycle of slow-varying large-scale structures that contain the modulation of some small-scale structures in the local speckle power.

In the K-distribution model, the gamma-distributed local power x is randomly determined over a certain time interval in which x has not changed perceptibly. Thus, such x can be considered as the integral of the power spectrum over all frequencies within that interval. As a result, the K-distributed model can be transformed into a model in frequency domain that describes the fluctuating Doppler spectrum as the product of the local power x and a suitable function of unit area [22]

$$S(\omega | x) = x \hat{S}(\omega) \quad (5.14)$$

$$\int_{-\infty}^{\infty} \hat{S}(\omega) d\omega = 1 \quad (5.15)$$

where $\hat{S}(\omega)$ itself can be modelled as a random Gaussian process similar to (5.4) in the following form

$$\hat{S}(\omega) = \frac{\exp\left(-(\omega - \omega_0)^2 / 2\sigma^2\right)}{\sqrt{2\pi\sigma^2}} \quad (5.16)$$

From (5.15) and (5.16), it is easy to understand that this model is based on the simple assumption that the frequency shift in all Doppler bins is identical. However, according to the observation on sea structures, larger frequency shifts usually occur on those of spike-like clutters. In order to make the power spectrum model more applicable, other than the speckle-like clutters, it is further associated with the spike-like clutters. Thus, the Doppler spectrum consists of two Gaussian components as below

$$S(\omega) = x_1 \frac{x_0 \hat{S}_0(\omega, \sigma_0, 0) + x_1 \hat{S}_1(\omega, \sigma_1, \Omega_1)}{x_0 + x_1} \quad (5.17)$$

$$\hat{S}(\omega, \sigma, \Omega) = \frac{\exp(-(\omega - \Omega)^2 / 2\sigma^2)}{\sqrt{2\pi\sigma^2}} \quad (5.18)$$

where x is the gamma-distributed local power that modulates the averaged clutter power over the frequency spectrum and Ω is the frequency shift from the center.

In (5.17), the first Gaussian component with a zero frequency displacement and relatively small power distribution, $\hat{S}_0(\omega, \sigma_0, 0)$, represents the speckle-like clutter from small-scale structures, while the second one with a frequency displacement from the center and a relative significant power distribution, $\hat{S}_1(\omega, \sigma_1, \Omega_1)$, represents the spike-like clutter from large-scale structures.

B. CLUTTER GENERATION PROCESSING

The sea clutter module developed emulates the sea clutter in terms of the amplitude and frequency displacement in the form of phase representation. Both the amplitude and phase information are then modulated into the gain and phase coefficients. Thus, new gain and phase coefficients are produced by changing (3.9) and (3.13) into

$$\phi_T(r, n) = \text{angle} \left(\text{real} \{T'(r, n) + \text{Clutter}'(r, n)\}, \text{imag} \{T'(r, n) + \text{Clutter}'(r, n)\} \right) \quad (5.19)$$

$$T'_N(r, n) = \frac{|T'(r, n)| + |\text{Clutter}'(r, n)|}{\max(|T'(r, n)|, |\text{Clutter}'(r, n)|)} \quad (5.20)$$

Figure 17 shows the block diagram of the modified DIS design integrated with the sea clutter module.

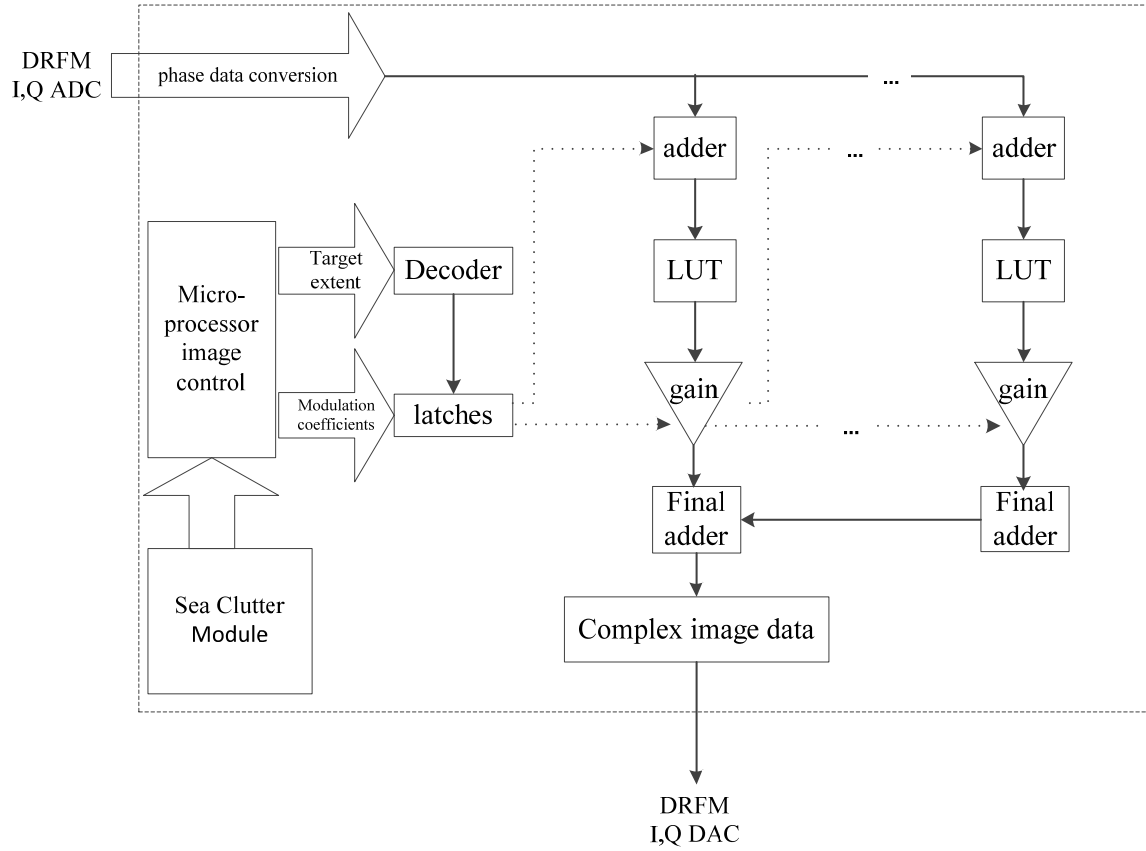


Figure 17. DIS Block Diagram with Sea Clutter Module.

1. Gain Coefficient Generation

The generation of the gain coefficient of the sea clutter module is similar to what has been described in Chapter III, with the target-profile amplitude replaced by the amplitude of the sea clutter, which is generated as follows.

According to the K-distributed model, the sea clutter can be statistically expressed by a combination of the gamma and Gaussian components with an additional clutter modulation in power on the gamma component [23]. A block diagram depicting the processing of generating the K-distributed clutter is shown in Figure 18.

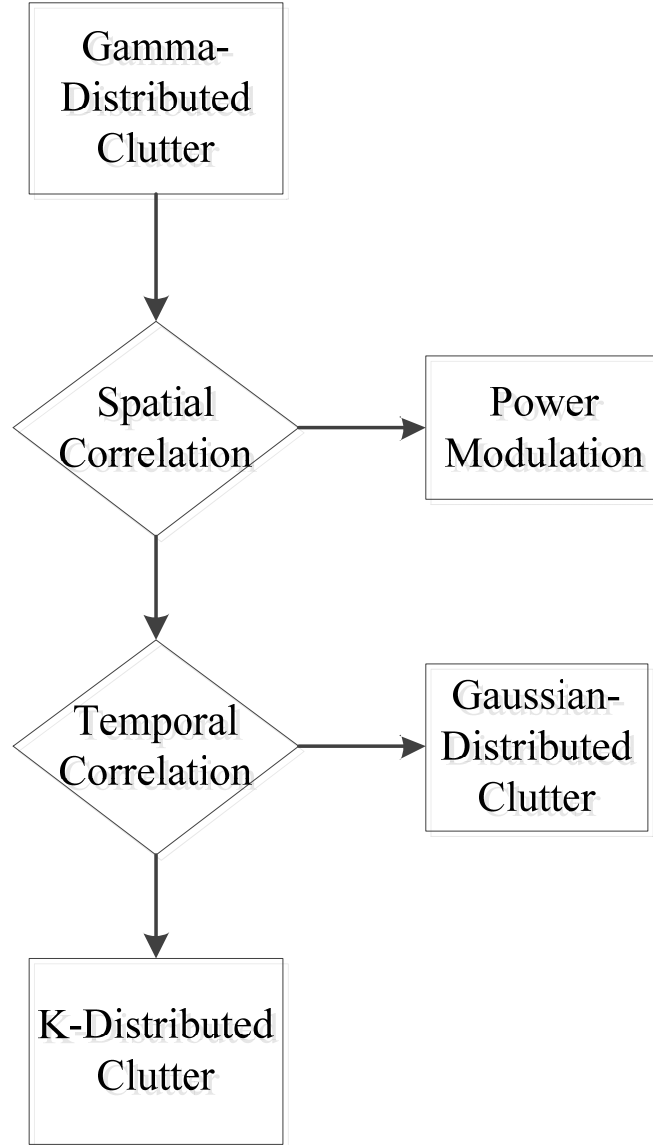


Figure 18. Block Diagram of K-Distributed Clutter Generation Process.

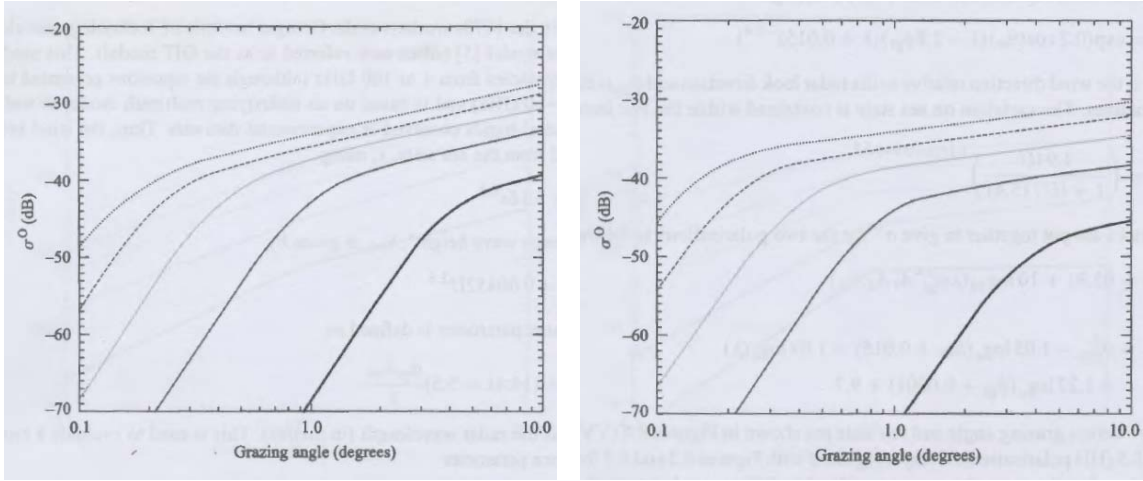
The RCS value for each individual clutter is randomly assigned based on an empirical RCS model developed by the Georgia Institute of Technology (GIT). This model is also known as the GIT model. This GIT model determines the relationship of the normalized clutter RCS versus grazing angle and sea state through wave tank experiments for radars of frequency ranging from 1 to 100 GHz. From the trend observed in the experimental data sets, the clutter RCS for horizontal and vertical can be approximately expressed as [25]

$$\sigma_H^0 = 65.91 + 10 \log_{10} (\lambda \phi_{gr}^{0.4} A_i A_u A_w) \quad (5.21)$$

$$\sigma_V^0 = \sigma_H^0 - 1.05 \ln(h_{ave} + 0.015) + 1.09 \ln(\lambda) + 1.27 \ln(\phi_{gr} + 0.0001) + 9.7 \quad (5.22)$$

where λ is the radar wavelength, ϕ_{gr} is the grazing angle, A_i is the sea state dependency parameter, A_u is the wind direction parameter, and A_w is the multipath interference parameter.

Figure 19 shows the experimental result at 9.5 GHz for sea state 1 through 5, in which most of the RCS values fall into the range between -30 dB and -40 dB for both polarization at low grazing angle (less than 10 degrees) [22]. Thus, in the simulation, the clutter RSC value is randomly chosen in the range between -20 to -40 dB to be more flexible to various sea state conditions and antenna polarizations.



a. Vertical polarization

b. Horizontal polarization

Figure 19. Normalized RCS Versus Grazing Angle from GIT Model for Sea States 1 to 5 (in the Order of Bottom to Top) (From [22]).

According to (5.1) and (5.2), the number of the clutter is directly related to the intensity of the gamma-distributed clutter. Thus, in the sea clutter module, the number of the clutter within each range-Doppler cell is assigned by a random integer, which is intended to reflect the environmental variation. The mean local power, x , is then obtained through a MATLAB built-in gamma random function with the consideration of

the clutter RCS and distance between the false target and the radar. By the same token, the Gaussian-distributed clutter can also be obtained through a MATLAB built-in Gaussian random function based on x , and thus the final K-distributed clutter is generated.

According to (3.7) and (3.8), the amplitudes of this K-distributed clutter for each range-Doppler and range cells are obtained as follows

$$Clutter(r, d, n) = A_{clutter}(r, d) e^{-j2\pi f_{clutter}(r, d)nPRI} \quad (5.23)$$

$$Clutter'(r, n) = \sum_{d=1}^{Nd(r)} Clutter(r, d, n) \quad (5.24)$$

where $A_{clutter}(r, d)$ is the amplitude of the K-distributed clutter and $f_{clutter}(r, d)$ is the corresponding frequency displacement discussed in the next section. The gain coefficient can be obtained through the normalization process through (5.20), (5.23), (5.24), and Table 1. Figure 20 shows the normalized amplitude range profile for the clutter generated. A plot of the function $Y = 1/R^2$ marked in red is also included for a comparison purpose.

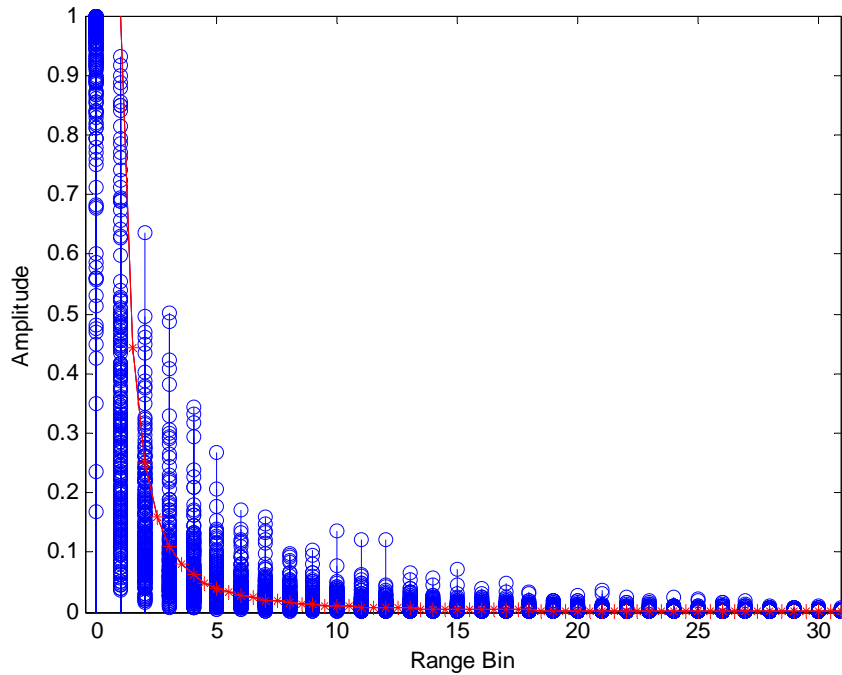


Figure 20. Normalized Amplitude Range Profile of the Sea Clutter.

With a closer examination on both Figure 20, it is clear that the amplitude of the clutters decreases dramatically in a behavior similar to that of the function $Y = 1/R^2$. Such similarity is corresponding to the relationship between the power of the clutter and the distance, $x \propto 1/R^4$, as described in (5.6). It implies that the amplitude of the clutters generated is appropriate for the production of the gain coefficient for the clutter.

2. Phase Coefficient Generation

The generation of phase coefficient in the sea clutter module is based on the same schemes to generate the DIS phase coefficient. The first step is to assign a frequency displacement for each clutter contained within a range-Doppler cell, so that the phase information of the clutter is obtained by taking the angle function on the clutter signal. In order to cooperate with the DIS and DRFM system, such phase information must also be quantized to fit the DRFM architecture.

Although a theoretical model for a power spectrum is presented in the previous section, the determination of the frequency displacement for the sea clutter through this model is far complicated. An empirical model based on the analysis of the data collected from radar surveillance operations and wave tank experiments is adopted instead to simplify the processing of random frequency displacement generation instead.

According to the experimental data from [22], [23], and [26], the empirical model is suggested to estimate the frequency displacement of the sea clutter for low grazing angles. It is found that the Doppler velocity at peak of the upwind spectrum appears to be approximately determined by the velocity of the wind speed for both polarizations in the following linear forms [26]

$$V_{D_vertical} \sim 0.25 + 0.18U \quad or \quad (5.25)$$

$$V_{D_horizontal} \sim 0.25 + 0.2U \quad (5.26)$$

where U represents the wind speed in meters per second. Since there is little difference between both polarizations, (5.26) is used to calculate the Doppler velocity value, V_D , in the sea clutter module, and the frequency displacement can easily be determined by

$$f_D = \frac{2V_D}{\lambda_{radar}} \quad (5.27)$$

here λ_{radar} represents the radar wavelength depending on the radar frequency. Table 2 shows the approximate upwind frequency displacements measured by radars of 1 and 10 GHz for sea state 1 to 4 by using (5.26) and (5.27).

| | Wind Speed (kn) | Wind Speed (m/s) | V_D ~0.25+0.2U | f_D ($\lambda=0.3m$) | f_D ($\lambda=0.03m$) |
|------------|--------------------|---------------------|---------------------|-----------------------------|------------------------------|
| Sea State1 | 0-6 | 0-3.0867 | 0.25-0.5873 | 1.66-5.78 | 16.6-57.8 |
| Sea State2 | 6-12 | 3.0867-6.1733 | 0.8673-1.4847 | 5.78-9.898 | 57.8-98.98 |
| Sea State3 | 12-15 | 6.1733-7.7166 | 1.4847-1.7933 | 9.898-11.955 | 98.98-109.55 |
| Sea State4 | 15-20 | 7.7166-10.2888 | 1.7933-2.0378 | 11.955-15.385 | 109.55-153.85 |

Table 2. Upwind Frequency Displacement under Various Sea States

When the wind turns from upwind to crosswind and to downwind, the frequency displacement shifts correspondingly from more positive displacement to zero and to negative value. Thus, the frequency for a clutter is randomly assigned as either positive or negative to represent the effect under the wind direction. An example of the code segment used for generating the frequency displacement for sea state 4 is shown below to illustrate the implementation of this frequency empirical model.

%GENERATION OF FREQUENCY DISPLACEMENT

```

if rand(1)<=0.5                                %assign random wind direction
    clutter_freq=randi([-110,-100],[1,1])+2*randn(1,1); %negative frequency for downwind
else
    clutter_freq=randi([100,110],[1,1])+2*randn(1,1); %positive frequency for upwind

```

From the code segment listed above, the Doppler frequency of the clutter is chosen from a frequency spectrum constructed by a statistical Gaussian random function. The mean of the Gaussian random function is determined by the sea state, the radar wavelength, and the wind direction. The Gaussian standard deviation, on the other hand, is determined by the choosing a value of 2 in order to include 95% of the frequency within the spectrum. It is also assumed that all clutters have a non-zero Doppler for a more general module.

Clutter observed by a 10GHz radar under sea state 4 is generated and a pulse-to-pulse correlation is performed as shown in Figure 21 and demonstrates the correct drop off rate expected. The Doppler amplitude spectrum for range cell 1, 5, 10, and 20 are examined as shown in Figure 22 to Figure 25. The amplitude frequency spectrum is obtained by taking the Fourier transform on the clutter signals contained within one range cell. Therefore, the characteristic of decreasing in amplitude is reflected in the figures when they are compared in the amplitude domain.

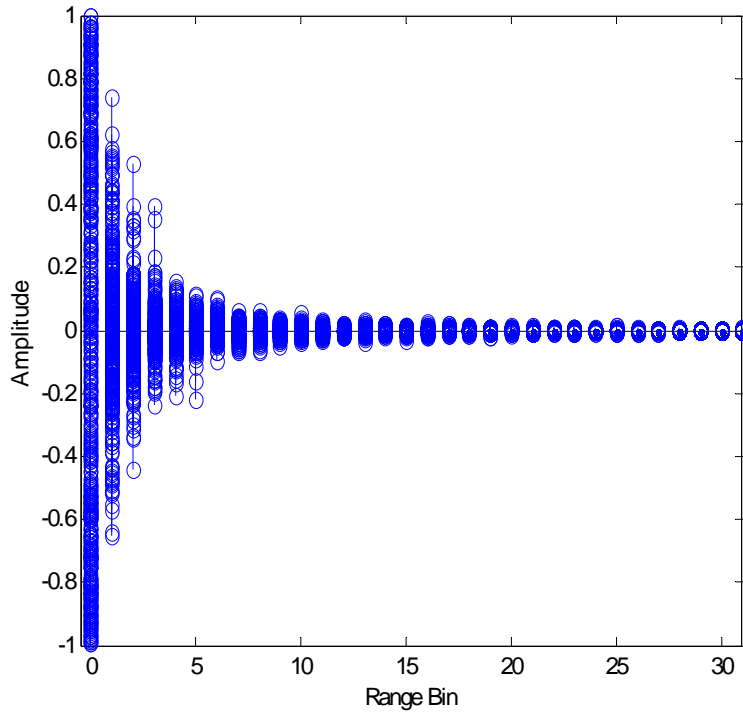


Figure 21. Pulse-to-Pulse Correlation on the Clutter Generated.

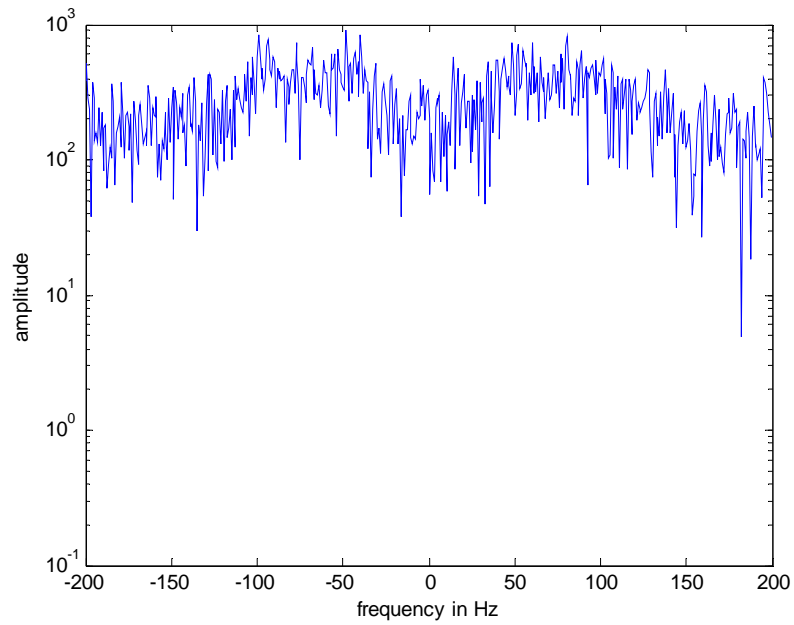


Figure 22. Amplitude Frequency Spectrum at Range Cell 1.

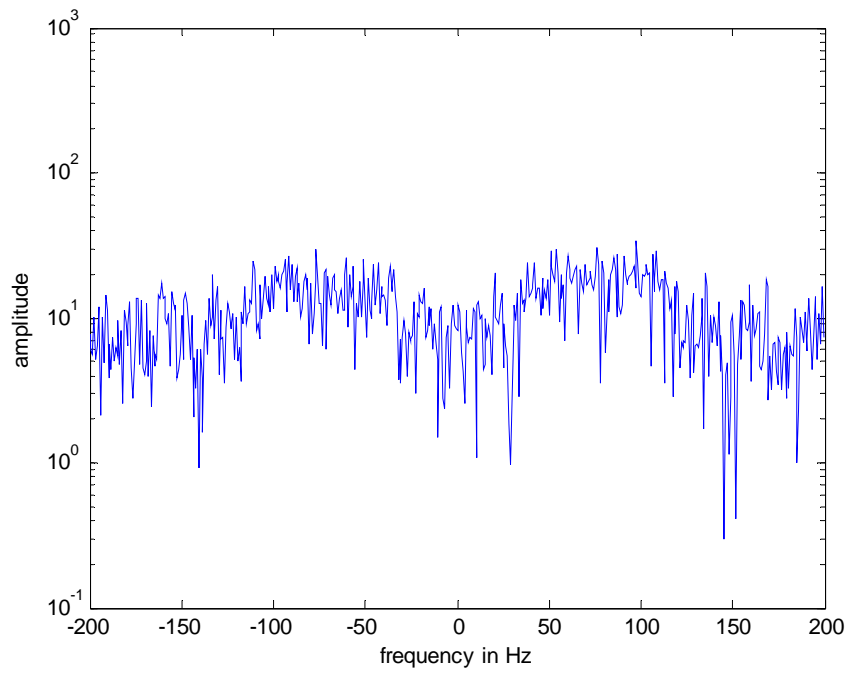


Figure 23. Amplitude Frequency Spectrum at Range Cell 5.

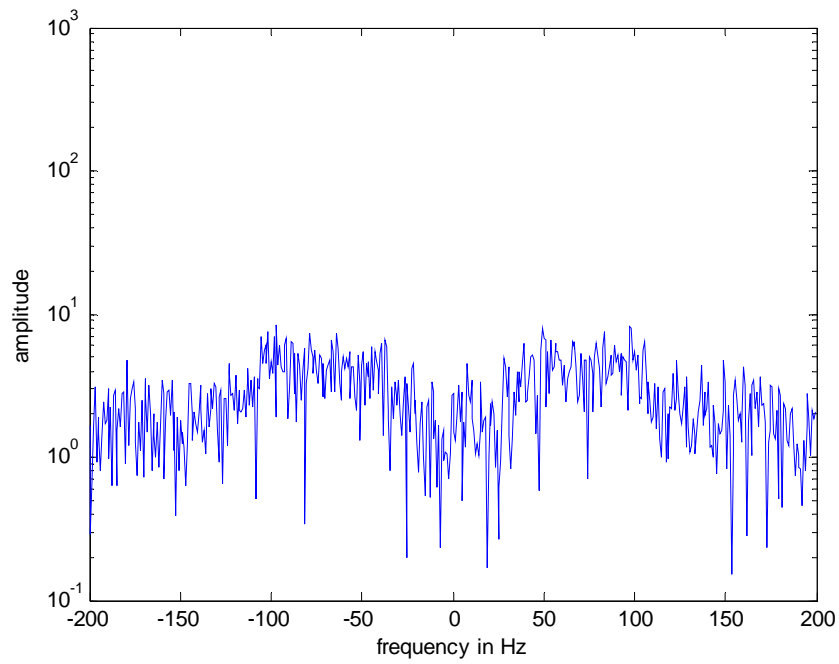


Figure 24. Amplitude Frequency Spectrum at Range Cell 10.

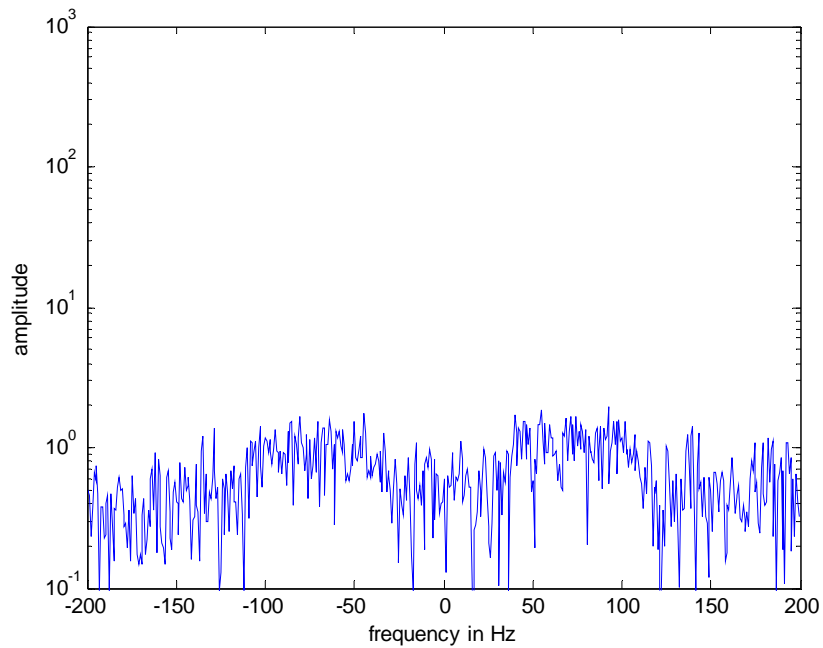


Figure 25. Amplitude Frequency Spectrum at Range Cell 20.

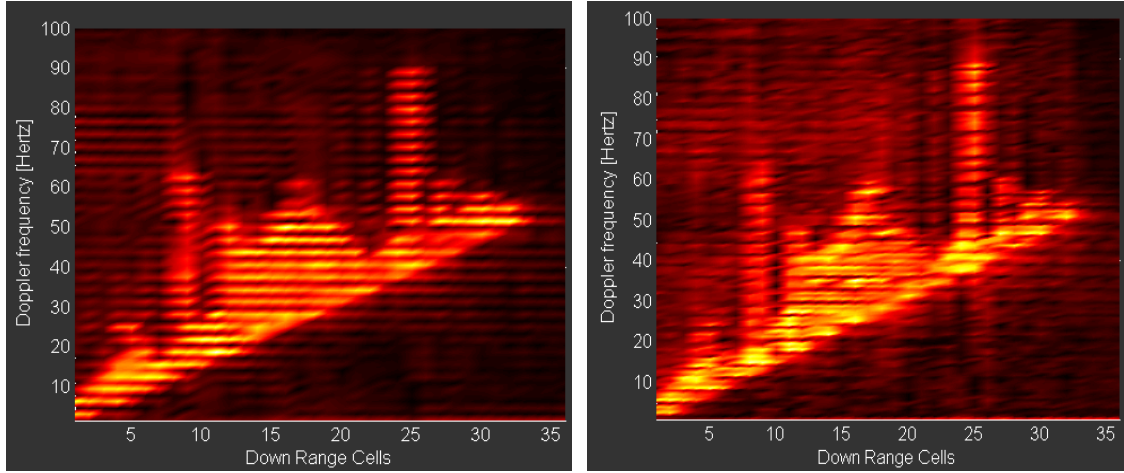
According to Table 2, the mean of the Gaussian random function is chosen approximately either between 100 and 110 or between -110 and -100. As a result, the center of the corresponding frequency spectrum is most likely between 50 and 100 in both positive and negative.

The spike-like clutters with stronger energy level can be recognized in Figure 22, and their frequency values are found to be slightly different. Such difference could possibly be due to the correlation with the speckle-like clutters. The speckle-like clutters, on the other hand, have the frequency values spread through the spectrum with weaker energy. This suggests that such clutters travel for a certain amount of time and do not change if observed within a relatively short period of the time. In either case, the frequency displacement generated for the clutter with this empirical model is appropriate to represent the Doppler shift of a random clutter.

C. SIMULATION RESULT

1. Evaluation on Performance of the Modified DIS Design

Figure 26 shows two ISAR images from the simulations based on an identical false-target profile of a ship with 32 by 256 range-Doppler cells. The image for the profile generated by the original DIS refers to Figure 26a, while that for the profile generated by the DIS incorporated with the sea clutter module is in Figure 26b. Although both images are discontinuous in the Doppler domain, which is inevitable due to the quantization of the phase into integer representation, it is clear to see that Figure 26b shows better continuity in both range and cross-range domains than Figure 26a.



a) Original DIS

b) DIS Modified with Sea Clutter Module

Figure 26. ISAR Image Simulation for DIS and Modified DIS.

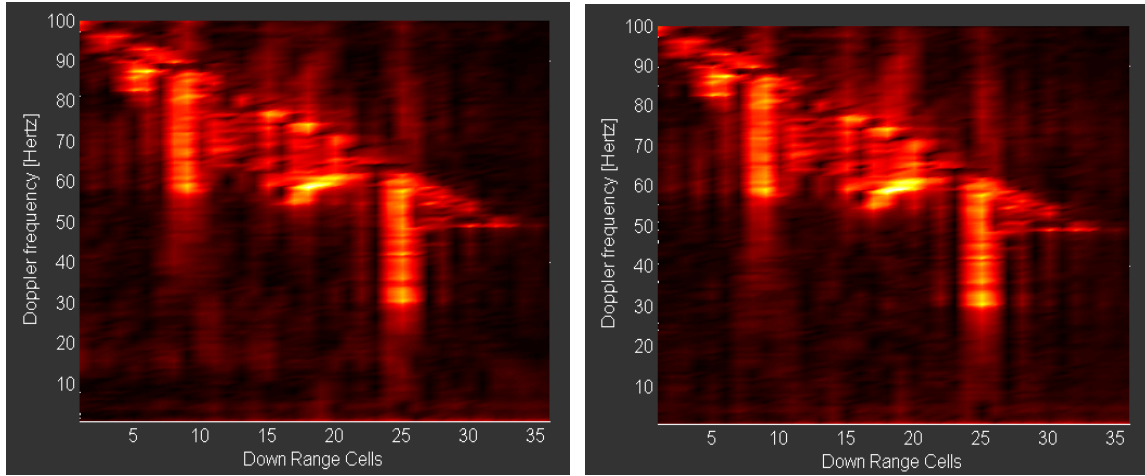
Also, notice that in the Doppler domain of the image in Figure 27b, there are some background noises forming in a shape similar to the ship around the structures with larger frequency shifts like the mast. This is the effect due to the correlation between the false-target and the sea clutter, which is the purpose behind incorporating the original DIS design with a sea clutter module.

2. The Impact of Radar Wavelength

According to (5.27), the frequency displacement generated by the empirical model has an inverse relationship with the radar wavelength. The purpose of this simulation is to examine how the radar wavelength could have impact on the empirical model and the modified DIS as well.

Figure 27 shows two ISAR images from the simulations based on the false-target profile of a ship that rotates in negative frequency shifts against the radar with 32 by 256 range-Doppler cells. These negative shifts make the target image upside down. The false-target profiles used for generating these two images are identical except for the frequency displacement generated by the sea clutter module. The frequency displacement chosen for Figure 27a is based on a radar wavelength of 0.3 meters for sea state 4, which, according to Table 2, has either a positive value approximately between 12 and 16, or a negative

value approximately between -16 and -12. The frequency displacement chosen for Figure 28b, on the other hand, is based on a radar wavelength of 0.03 meters and has either a positive value approximately between 120 and 160, or a negative value approximately between -160 and -120.



a) Wavelength = 0.3m

b) Wavelength = 0.03m

Figure 27. ISAR Image for Modified DIS at Different Radar Wavelength.

With a closer inspection on both images, other than some variances of the background noise distribution, the majority of the false-target images are in great similarity. In other words, the frequency empirical model used to generate the frequency displacement has little relationship with the radar wavelength (or frequency) on which ISAR usually operates.

3. The Impact of Sea State

The sea state is one of the most critical environmental variables that can greatly affect the RCS characteristic of the sea clutter. As suggested from Table 2, the higher the sea state, the more complicated and rough the sea surface. In the models used for the sea clutter module, the generation of the clutter RCS and frequency displacement for the clutter is also involved with the sea state, and thus, this simulation is performed to examine if the false-target profile with the randomly assigned clutter RCS and frequency displacement produces a reasonable image in the same manner as varied sea state.

Figure 28 shows ISAR images from the simulations based on a false-target profile of a ship that rotates in negative frequency shifts against the radar with 32 by 256 range-Doppler cells for sea state 1 through 4. These negative shifts make the target image upside down. The intensity of the ship body and clutter is identical for all four images.

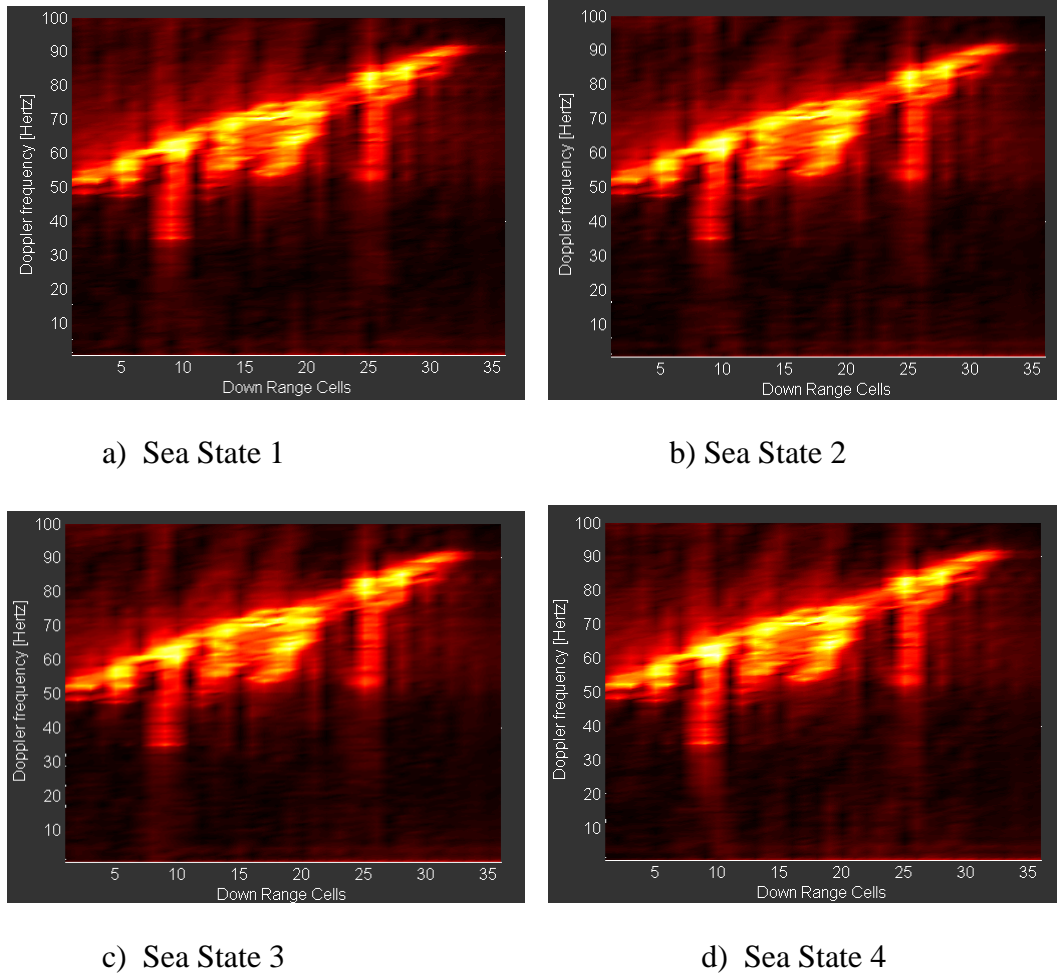


Figure 28. ISAR Image for Modified DIS at Different Sea State.

Such results suggest there is no tremendous difference in the clutter RCS with respect to various sea states for a low grazing angle, which corresponds with the observation from the experimental data, as shown in Figure 19. As far as the frequency displacement is concerned, the amount of clutter with a large frequency displacement increases as the sea state gets higher. Such clutter can be referred to as spike-like clutter caused by the increasing wind speed at higher sea state. Hence, the empirical models used

for generating the clutter RCS and frequency displacement are able to reflect a realistic behavior of clutter in accordance with the change in sea state.

D. CHAPTER SUMMERY

In the beginning of this chapter, different theoretical models used to statistically characterize the behavior of the sea clutter in amplitude and frequency displacement with respect to critical environmental parameters are presented. Next, an illustration is presented on how the sea clutter module generates sea clutter profiles compatible with the DIS signal processing to enhance the false-target signal through empirical models based on the theoretical methods. Finally, a series of discussions on the simulation results are provided to verify the performance of the novel modified DIS design and the reasonableness of the methodology for random clutter generation performed by the sea clutter module. The next chapter provides the thesis conclusions and concluding remarks.

THIS PAGE INTENTIONALLY LEFT BLANK

VI. CONCLUSION AND REMARKS

This thesis first introduces the ISAR imaging process followed by a discussion of the theoretical operation of electronic attack against ISAR, as well as the electronic protection of ISAR from the DRFM-based DIS false targets, through research. Next, a modified DIS design that incorporates a sea clutter module is introduced as an improved EA technique against ISAR. In order to generate reasonable sea clutter, several statistical sea clutter models are described, as well as the random processes used to generate the amplitude and frequency displacement coefficients that represent the random sea clutter. Finally, the simulation of the modified DIS design is executed to evaluate the performance of the new design. Several observations and remarks are concluded throughout the thesis and are described as follows.

A. CONCLUSION

The algorithm used to discriminate DRFM-based false targets with the pulse diversity technique could suppress the DRFM-based jamming signal up to -20 dB lower than the true radar returns and thus could easily reject the jamming signals sent from DRFM-based jammers. The DRFM penalizing algorithm, on the other hand, could suppress the jamming signal up to -40 dB lower than the true radar returns on the premise that the characteristic of the jammer is known beforehand. However, there is a great difficulty to obtain such information. Thus, the algorithm with the pulse diversity technique is much more flexible than the DRFM penalizing one even if it does not have the best performance against the DRFM-based jamming technique that covers the one derived from the DIS design.

With two identical radars operating at the same time, one in transceive mode and the other in receive-only mode, the cross-track interferometry scheme is able to locate the false target within a certain distance from the DRFM jammer platform through a spatial cancellation process on the output image of the two radars. Although both radars receive the false-target signal, it is the displacement between them that produces a delay, or a phase difference, that allows the cancellation process to partially locate the false target. In

order for the spatial cancellation to function properly, the false image must be carefully generated so that it has the slant range with respect to the transceiver radar approximately equal to that of the jammer platform. Such limitation reduces its flexibility against the DRFM-based false target. Nevertheless, the cross-track interferometry algorithm can be, in general, considered as an effective method to counter the DRFM-based false-target images, including those generated by the DIS.

Determining the continuity of the target image in cross-range domain is one of the most convenient methods to discriminate the DIS false target since it takes advantage of the flaw of the DIS design in the possible gap produced during the digitization process on the phase information, including the phase sampling of the intercepted ISAR signal and the phase coefficient generated by the DIS microprocessor. Such errors lead to the discontinuity of the image in cross-range domain, which makes the images less likely to be a real target. The design of the DIS false-target profile also contributes to this discontinuity. The modified DIS design proposed in this thesis adds a sea clutter effect to the DIS false target so that the interaction between the reflective surface of the target object and the background clutter is emulated. In addition, a series of simulations prove that the random Doppler shift of the sea clutter derived from the modified DIS design can be used to ease the discontinuity in cross-range domain.

B. RECOMMENDATIONS

There is still room for the MATLAB software to be improved by replacing some of the current iterative loop structures into matrix operation so that the performance of the parallel operations in DIS is increased and the simulation time is reduced, as well.

The amplitude and frequency displacement of the sea clutter is randomly generated through a Gaussian and gamma statistics model based on unified parameters, which may not be optimal. More research can be performed to identify a better setting for the parameters of the related statistic model. Hence, the amplitude and frequency displacement of the clutter can be assigned with an even more realistic value.

LIST OF REFERENCES

- [1] P.E. Pace et al., "Digital false-target image synthesiser for countering ISAR," *Proc. IEE Radar, Sonar and Navig*, vol. 149, pp. 248–257, Oct. 2002.
- [2] F. Berizzi, "ISAR imaging of targets at low elevation angles," *IEEE Trans. Aerosp. Electron. Syst.*, vol. 37, pp. 419–435, 2001.
- [3] Rongbing Gan, YuLing Liu and Zhenghong Yi, "Primary exploration on ISAR image deception jamming," in *Proceedings of the 1st Asian and Pacific Conference on Synthetic Aperture Radar*, 2007, pp. 83–86.
- [4] Hongya Liu and Xin Jia, "Methods to recognize false target generated by digital-image-synthesiser," in *Proceedings of the 2008 International Symposium on Information Science and Engineering*, 2008, pp. 71–75.
- [5] F. A. Le Dantec, "Performance analysis of a digital image synthesizer as a counter-measure against inverse synthetic aperture radar," M.S. thesis, Dept. Elect. Comput. Eng., Naval Postgraduate School, Monterey, CA, 2002.
- [6] Changyong Jiang et al., "Design of high-speed DRFM system," in *2009 World Congress on Computer Science and Information Engineering*, 2009, pp. 582–586.
- [7] P. E. Pace, *Advanced Techniques for Digital Receivers*. Boston, MA: Artech House, 2000.
- [8] M. I. Skolnik, *Introduction to Radar Systems*. Boston: McGraw Hill, 2001.
- [9] S.D. Berger, "Digital radio frequency memory linear range gate stealer spectrum," *IEEE Trans. Aerosp. Electron. Syst.*, vol. 39, pp. 725–735, 2003.
- [10] Bo Tang, Jun Tang and Ying-ning Peng, "Research on deception jamming for countering ISAR," in *Proceedings of the 2009 IET International Radar Conference*, 2009, pp. 1–4.
- [11] A.W. Deorry, "Ship dynamics for maritime ISAR imaging," Sandia National Laboratories, Albuquerque, NM, Tech. Rep. SAND2008–1020, Feb. 2008.
- [12] Naval Research Laboratory website, <http://radar-www.nrl.navy.mil/Areas/ISAR/>.
- [13] D. C. Schleher, *Electronic Warfare in the Information Age*. Boston: Artech House, 1999.
- [14] P.E. Pace, D.J. Fouts and D.P. Zulaica, "Digital Image Synthesizers: Are Enemy Sensors Really Seeing What's There?" *IEEE A&E Systems Magazine*, vol. 21, pp. 2–2, Feb. 2006.
- [15] Chen Li and Daiyin Zhu, "The detection of deception jamming against SAR based on dual-aperture antenna cross-track interferometry," in *IEEE Radar Conference*, 2006, pp. 1–4.

- [16] D.J. Fouts et al.,(2002, Jun), "A single-chip false target radar image generator for countering wideband imaging radars," *IEEE Solid-State Circuits*, vol. 37, no. 6, pp. 751–759.
- [17] Yuan Li, Xue-mei Luo and Ga-huan Lv, "The study of multi-false targets synthesizing technology against chirp ISAR," in *Proceedings of International Conference on Microwave and Millimeter Wave Technology*, 2008, pp. 802–805.
- [18] Feng Zhu et al., "A new method of camouflage jamming against ISAR based on compensating modulation," in *Proceedings of the 8th International Symposium on Antennas, Propagation and EM Theory*, 2008, pp. 422–425.
- [19] M. Soumekh, "SAR-ECCM using phase-perturbed LFM chirp signals and DRFM repeat jammer penalization," *IEEE Trans. Aerosp. Electron. Syst.*, vol. 42, pp. 191–205, 2006.
- [20] M. Soumekh, "SAR-ECCM using phase-perturbed LFM chirp signals and DRFM repeat jammer penalization," in *Proceedings of 2005 IEEE International Radar Conference*, 2005, pp. 507–512.
- [21] J. Akhtar, "An ECCM scheme for orthogonal independent range-focusing of real and false targets," in *IEEE Radar Conference*, 2007, pp. 846–849.
- [22] K. D. Ward, R. A. Tough, S. Watts, Institution of Electrical Engineers and Institution of Engineering and Technology, *Sea Clutter : Scattering, the K-Distribution and Radar Performance*. London: Institution of Electrical Engineers, 2006.
- [23] K. D. Ward, "Compound representation of high resolution sea clutter," *Electronics Letters*, vol. 17, pp. 561–563, 1981.
- [24] S.P. Watts et al., "The physics and modelling of discrete spikes in radar sea clutter," in *Proceedings of the 2005 IEEE International Radar Conference*, 2005, pp. 72–77.
- [25] F. Totir, E. Radoi and A. Quinquis, "Multidimensional superresolution ISAR reconstruction techniques in sea-cluttered environment," in *2005 Oceans - Europe*, 2005, pp. 44–49, vol. 1.
- [26] A.M. Raynal and A.W. Doerry, "Doppler characteristics of sea clutter," SandiaNational Laboratories, Albuquerque, NM, Tech. Rep. SAND2010–3828, Jun. 2010.

INITIAL DISTRIBUTION LIST

1. Defense Technical Information Center
Ft. Belvoir, Virginia
2. Dudley Knox Library
Naval Postgraduate School
Monterey, California
3. Chairman
Department of Information Science
Naval Postgraduate School
Monterey, California
4. Dr. Phillip Pace
Department of Electrical and Computer Engineering
Naval Postgraduate School
Monterey, California
5. Dr. Douglas Fouts
Department of Electrical and Computer Engineering
Naval Postgraduate School
Monterey, California
6. Maj. Lin, Yowchyun
Taiwaness Air Force
Taipei, Taiwan